Uptake of Pb and formation of mixed (Ba,Pb)SO_4 monolayers on barite during cyclic exposure to lead-containing sulfuric acid

Benjamin. A. Legg[1], Sang Soo Lee[2], Juan C. Garcia[2], Hakim Iddir[2], Tim T. Fister[2], Vijayakumar Murugesan[1*]*

1. Physical Sciences Division, Pacific Northwest National Laboratory, Richland WA, USA.
2. Chemical Sciences and Engineering Division, Argonne National Laboratory, Lemont, IL 60439 USA.

Keywords: Energy storage, batteries, crystal growth, nucleation, epitaxy

Abstract: Barite ($BaSO_4$) is a common additive in lead-acid batteries, where it acts as a nucleating agent to promote the reversible formation and dissolution of $PbSO_4$ during battery cycling. However, little is known about the molecular-scale mechanisms that control the nucleation and cyclic evolution of $PbSO_4$ over a battery's lifetime. In this study, we explore the responses of a barite (001) surface to cycles of high and low lead concentrations in 100 mM sulfuric acid solution using in-situ atomic force microscopy and high-resolution X-ray reflectivity. We find that $PbSO_4$ epitaxial films readily nucleate on the barite surface, even from solutions that are undersaturated relative to bulk $PbSO_4$. Despite this, barite (001) proves to be an ineffective nucleator of bulk

$PbSO_4$, as multilayer growth is suppressed even in highly supersaturated solutions. Instead, we find evidence that Pb^{2+} ions can directly exchange with Ba^{2+} to create mixed $(Ba,Pb)SO_4$ surfaces. These chemically mixed surfaces do not host $PbSO_4$ monolayers as readily as pristine barite, and the original reactivity is not regained until a fresh surface is reestablished by aggressive etching. Our results can be partly explained by traditional models of thin-film growth, which predict a Stranski-Krastanov (S-K) growth mode, where monolayer films are stabilized by a reduction in surface energy, but multilayer growth is inhibited by epitaxial strain. Complementary density functional theory calculations confirm the basic energetic-terms of the model, but also show evidence for thickness-dependent energetics that are more complex than would be predicted from traditional models. The experimental results are better understood by extending the model to consider the formation of mixed surfaces and films, which have reduced strain and interfacial energies relative to pure films, while also being stabilized by entropy of mixing. These insights into non-stoichiometric heteroepitaxy will enable better predictions of how barite affects $PbSO_4$ nucleation in battery environments.

1. Introduction

Lead acid batteries are often associated with pulsed power applications or industrial uninterruptible power systems, but their low cost is attractive for emerging long duration storage applications. For lead batteries to compete in this market, they will require improved cycling, ideally at greater depth of discharge.[1] Understanding and controlling the atomic-scale processes governing growth and dissolution of $PbSO_4$, the discharge product in a lead acid battery, is central toward achieving higher utilization and cycle-life.[2] One route toward tailored or directed $PbSO_4$ crystal growth is to use a nucleation promoting additive. Barite ($BaSO_4$) particles are a common expander component in the negative electrodes of lead-acid batteries,[3, 4] where they serve as a

nucleating agent to guide the reversable nucleation, growth, and dissolution of $PbSO_4$ during battery cycling. Past work shows that barite can reduce the overpotential needed to nucleate $PbSO_4$,[4] provide preferential sites for $PbSO_4$ nucleation,[5] and improve battery cycle life.[6] However, barite can also introduce challenges for battery recycling, which is essential for capturing spent lead.[7] Barite's effectiveness is generally attributed to the fact that it is isostructural with the $PbSO_4$ phase anglesite, which allows $PbSO_4$ to nucleate on barite as an epitaxially matched precipitate, with energy barriers that are expected to be reduced relative to homogenous nucleation in bulk solution.[8] However, the molecular scale interactions between $PbSO_4$ and barite are complex and poorly understood, especially in the sulfuric acid solutions that are relevant to lead-acid batteries. Better understanding of such processes will aid in ongoing efforts to produce improved battery additives[9,10] and build models of battery operation.[11] We hope this work will help address emerging grid-level power storage needs by facilitating the development of lead-acid batteries with improved efficiency, cycle-life, and recyclability.

The complexity of lead-barite interactions has been demonstrated by recent work aimed at understanding the environmental behavior of lead in neutral aqueous solutions. Bracco et al.[12] demonstrated that Pb^{2+} ions can directly interact with barite (001) through two major modes: forming inner-sphere adsorbates and exchanging with Ba^{2+} to incorporate into the topmost layer of barite. Some evidence for surface precipitation was also observed, but the specific phases were unidentified. Thus, there are important unanswered questions about how Pb sorption and incorporation are coupled to precipitation of phases such as $PbSO_4$. Moreover, these processes may change in sulfuric acid solution, where high sulfate concentrations reduce the amounts of $BaSO_4$ and $PbSO_4$ that will dissolve, and low pH inhibits the formation of hydroxide and carbonate phases (which were a concern at neutral conditions).

An additional complexity is that epitaxial relationships between anglesite and barite may cause deviations from the most commonly used models of heterogenous nucleation, such as Turnbull's hemispherical cap model[13]. Studies of similar heteroepitaxial pairs such as $BaCrO_4$ on $BaSO_4$ [14], $SrSO_4$ on $CaSO_4$ [15], $SrSO_4$ on $BaSO_4$ [16], $PbSO_4$ on $SrSO_4$ [17], and most recently $PbSeO_4$ on $BaSO_4$[18] have shown that epitaxial strain can induce a diversity of complex nucleation and growth modes. Depending on the relative values of the surface energies and the lattice mismatch, the active mode may be Volmer-Weber (V-W), Frank Van der Merwe (F-VdM), or Stranski-Krastanov (S-K) growth. S-K growth is a particularly interesting mode that involves mixtures of 2D films and 3D islands. It occurs when the precipitating phase has a lower interfacial energy than the substrate and thus wets to form a 2D film at small coverages, but where a large epitaxial strain inhibits the formation of multilayer epitaxial films. To relieve this strain, multilayer films in the S-K regime tend to form islands rather than continuous films. Based on their surface tensions and structural relationships (which we shall discuss at length later in this paper), we anticipate that S-K growth is likely for anglesite on barite, but this has not previously been investigated in detail.

A final complexity is the time-evolution of lead-barite interactions. Processes of sorption, incorporation, nucleation, and growth occur on diverse timescales. Rapid processes of ion physisorption may be coupled to slower processes, such as the structural incorporation of impurity ions, or to more complex processes such as nucleation and growth. Thus, we should expect reactivity to evolve over time. For example, as ion exchange gradually changes the composition of the barite surface, it may alter the propensity for later $PbSO_4$ nucleation and growth. Understanding the interaction between these processes will be critical to evaluating barite's effectiveness as a nucleator during repeated exposure to acidic lead-containing electrolytes, as would occur during battery cycling.

To understand how the concurrent processes of Pb^{2+} sorption, incorporation, and precipitation occur on barite, we apply two advanced surface-specific experimental techniques: in situ atomic force microscopy (AFM), and high-resolution X-ray reflectivity (XR). We focus on interactions of $Pb^{2+}$with the barite (001) surface since it is a dominant cleavage plane and growth surface that is highly expressed for most barite crystals. We utilize 100 mM sulfuric acid as an experimentally tractable acid concentration that allows us to approximate the dilute limit of battery conditions. In situ AFM provides sub-nanometer imaging of the barite interface that allows us to track morphological changes in real time and understand how molecular-scale surface features such as steps and terraces influence nucleation and growth processes. In situ XR provides a detailed characterization of surface structure and composition, including crystallographic relaxation of the barite surface, sorption of lead onto the surface, and incorporation of lead into the surface.

Finally, we present a thermodynamic model that allows us to predict how epitaxial strain and surface energies influence the driving-force for impurity incorporation and overgrowth of epitaxial films. Our model moves beyond simple models of epitaxial growth to consider films and surfaces of mixed composition. The model parameters, such as strain energy and surface tension are informed by a series of density functional theory (DFT) calculations, and the results allow us to understand the complex pathways that Pb^{2+} ions interact with the barite surface in sulfuric acid solutions.

2. Materials and Methods

All experiments were performed on barite crystals from a geode from Sichuan, China. The crystals were a few millimeters in size and had a bladed habit (a mounted crystal is shown in SI Figure S1). X-ray fluorescence data measured at beamline 33-BM-C of the Advanced Photon Source (APS) in Argonne National Laboratory indicates that the crystals are greater than 99.9 at.

% purity in cation content, with Sr as the major impurity at <0.1 at. % (see Figure S2). Before each experiment, the crystals were cleaved to produce fresh (001) surfaces that are clean and atomically flat, and thus well-suited for AFM and XR studies.

2.1 Atomic Force Microscopy.

For in situ AFM experiments, concentrated sulfuric acid (H_2SO_4, 98 wt.%, Fisher Scientific) was diluted in ultrapure deionized water (DiW) (18.2 MΩ·cm) to produce a 200 mM H_2SO_4 stock and lead nitrate ($Pb(NO_3)_2$, ≥99.9% from Sigma-Aldrich) was dissolved in DiW to produce a 100 mM $Pb(NO_3)_2$ stock. Lead-containing 100 mM sulfuric acid solutions were produced by diluting the $Pb(NO_3)_2$ stock with DiW to a concentration of twice the final experimental value, and then mixing in equal portions with 200 mM sulfuric acid a few minutes prior to the experiments. This sequence reduces the chance for inadvertent nucleation of crystals that can occur when preparing supersaturated solutions.

AFM was performed using a Cypher VRS (Oxford Instruments) with a liquid perfusion holder. Immediately before imaging, each barite sample was cleaved, blown clean with N_2 gas, and mounted on a steel puck using Crystalbond 509 adhesive (SI Figure S1). The sample was rinsed several times with lead-free 100 mM sulfuric acid by pipet before adding a small droplet (roughly 50 µL) and sealing the AFM cell (SI Figure S3). In-situ imaging was performed in the resulting liquid meniscus. To protect the instrument, H_2SO_4 concentrations were limited to 100 mM, despite the battery-relevance of higher concentrations. Imaging was performed with gold-coated Arrow-UHF AuD probes, which were mounted using PEEK clamps to avoid corrosion couples. Imaging was performed in amplitude-modulated mode with blueDrive^{TM} photothermal excitation, while recording both height and phase-shift channels. Excitation amplitudes were adjusted between 1 nm (for imaging atomic-scale structure) to 10 nm (for imaging micron-scale areas with nm-scale

steps). In each experiment, the AFM operating parameters were optimized while imaging in lead-free 100 mM H_2SO_4, and then the Pb-containing solutions were applied via PTFE tubing and a infuse/withdraw syringe pump (PhD Ultra, Harvard Apparatus) at a flow rate of 0.1 mL/min, while imaging in real time. After all experiments, the sample holder's working surfaces and tubing were cleaned with dilute nitric acid to prevent accumulation of lead residues.

2.2 X-ray Reflectivity.

For XR experiments, a 100 mM sulfuric acid solution at pH ~1 was prepared by diluting concentrated sulfuric acid (98 wt.%, Fisher Scientific) in DiW. The lead-containing sulfuric acid solutions were prepared by diluting a 100 mM $Pb(NO_3)_2$ stock solution to $[Pb]_{tot}$ = 9 µM using the 100 mM sulfuric acid. The barite-saturated solution (BSS) was prepared by equilibrating DiW with barite ($BaSO_4$) powder on a shaker table (~200 rpm) for more than one month, after which solid particles were removed by filtration. This BSS has an equal concentration, ~10 µM, of [Ba] and $[SO_4^{2-}]$ estimated using the Geochemist's Workbench® with the MINTEQ database[19] at pH 5.6 (measured).

The freshly cleaved barite crystal was placed initially in BSS encapsulated in a thin-film X-ray reflectivity cell[20]. The solution was replaced by flushing ~10 mL of lead-free 100 mM H_2SO_4, after which ~1 mL of the new solution was maintained in the cell for reaction with barite for ~40 min. After this reaction time, excess solution was drained to maintain a several-µm-thick solution layer on the barite surface for in-situ XR measurements (described in the next paragraph). After the measurements, the remaining solution was flushed by ~10 mL of 9 µM $Pb(NO_3)_2$ solution in 100 mM H_2SO_4. A small volume (~1 mL) of the new solution was maintained in the cell for reaction for ~30 min, after which excess solution was drained for in-situ XR measurements.

XR experiments were performed at beamline 33-ID-D of APS in Argonne National Laboratory. The monochromatic incident X-ray beam was focused by a toroidal mirror to a cross sectional dimension of ~0.1 mm (vertical, *v*) × 1.0 mm (horizontal, *h*) at the sample location with a flux of ~5×10^{12} photons/sec. In situ high-resolution XR data were collected in the specular geometry at photon energy, *E*, of 18.0 keV (i.e., wavelength, λ, = 0.689 Å) as a function of momentum transfer *Q*, defined as $4\pi\sin(2\theta/2)/\lambda = 2\pi L/d$, where 2θ is the angle between the incident and reflected X-rays, *L* is the Bragg index of the barite (001) reflection, and *d* = ~7.154 Å is the (001) layer spacing[21]. Each XR dataset was collected in the *Q* range from 0.21 to 5.72 $Å^{-1}$. XR data were analyzed by fitting to a multi-layer structural model consisting of solid barite, several layers of structurally relaxed barite at the interface, several layers of vertically structured interfacial solution, and a bulk solution above this interfacial region.[12, 21] Details of the fitting procedure are provided in SI Section 6. Additional in situ resonant anomalous X-ray reflectivity (RAXR) spectra were collected by tuning *E* around the X-ray L_{III}-absorption edge energy of Pb (E_{Pb} = ~13.05 keV) at a series of fixed *Q* ranging from 0.36 to 2.50 $Å^{-1}$. The RAXR spectra were initially fit using a model-independent approach to yield a semi-quantitative electron density profile of interfacial Pb, and then a detailed Pb distribution was attained by fitting the RAXR spectra to a model composed of a series of Gaussian-distributed Pb layers, as described in SI Section 6. These XR and RAXR measurements in the Pb-containing H_2SO_4 solution took ~3.5 h. The stability of the system and the reproducibility of the data were tested and confirmed by duplicate measurements at two different locations on the same sample surface.

2.3 Density Functional Theory.

Atomistic DFT simulations were applied investigate the energetic stabilities of the barite (001) surfaces with $PbSO_4$ layers. Simulations were performed using the Vienna Ab Initio Simulation

Package (VASP).[22,23] The exchange-correlation potentials were treated by the generalized gradient approximation (GGA) parametrized by Perdew, Burke, and Ernzerholf (PBE).[24] The interaction between valence electrons and ion cores was described by the projected augmented wave (PAW) method.[25] A rigorous set of parameters was used for all simulations to ensure derivation of accurate and consistent total energies. The wave functions were expanded in the plane wave basis up to a kinetic energy of 800 eV. The Brilliuon zone was sampled with a k-points density of at least 1000 points per atom. Bulk solvent effects were accounted for by using an implicit solvation model as implemented in VASP.[26,27] The simulation cells for surfaces were set to be at least twice as big in the a and b direction as the original MSO_4 cell (M=Ba, Pb), to allow for correct relaxion. There cells have 480 ions and at least ten monolayers in total thickness. A detailed description of the cells and procedures to compute the relevant properties is presented in SI Section 7.

3. Results and Discussion

3.1. Growth of Monolayer $PbSO_4$ Films on Barite.

AFM images of barite (001) in lead-free 100 mM H_2SO_4 revealed a flat surface with a typical triangular step and terrace morphology (see Fig 1a, t = 0 min).[28] The terraces are typically several microns wide, but we focus on regions with steps since they display richer phenomenology. Most step heights are ~3.5 Å, consistent with ½ unit cell thickness (i.e., d_{002} = 3.58 Å).[21, 29] The steps typically came in pairs, with each step separated by a few tens of nanometers. This pairing is due to barite's 2_1 screw axis in the [001] direction, which causes adjacent (002) terminations to have identical structure but opposite orientations,[29, 30] so that one face is preferentially exposed on cleaving.

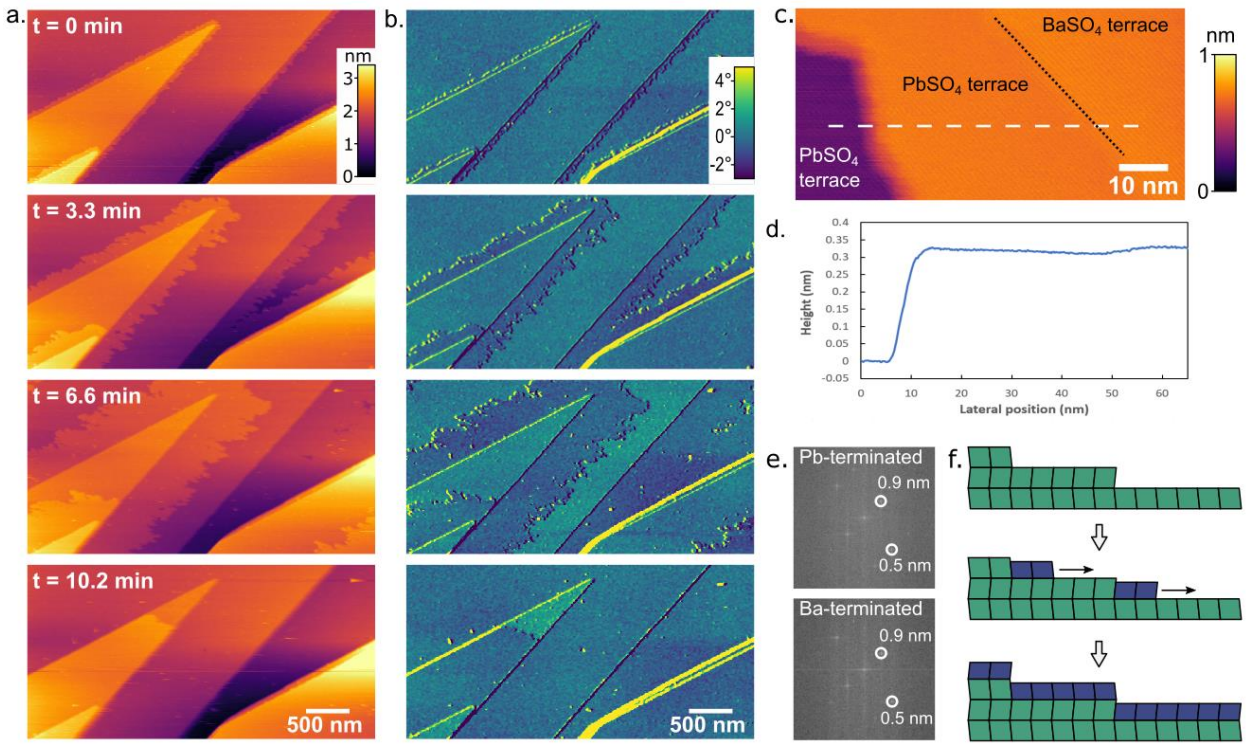

Fig 1: AFM imaging of lead-sulfate epitaxial overgrowth on barite (001). a. In-situ AFM height image sequence taken with ~ 3.3 min intervals, showing the nucleation of ~3.5 Å thick monolayer films at preexisting step edges on the barite (001) surface, and their propagation across terraces until the entire surface is covered with a monolayer of $PbSO_4$. **b.** Corresponding AFM phase-shift images, in which clear contrast is observed between the original $BaSO_4$ terminated surface and the $PbSO_4$ overgrowth. **c.** high-resolution AFM height image of three terraces: two $PbSO_4$ terminated terraces on the left and one $BaSO_4$ terminated terrace on the right, with lattice resolution visible. **d.** height line-profile across the three terraces shown in c, showing an ~ 0.33 nm step height between the $PbSO_4$ terminated terraces, and an increased thickness of ~0.02 nm for the BaSO4 terrace relative to the adjacent $PbSO_4$ terrace. **e.** Fast Fourier transforms (FFTs) obtained from subfigure c, showing that the $PbSO_4$ and $BaSO_4$ terminated surfaces have indistinguishable periodicities of ~9 Å and ~5 Å. **f.** Schematic of the indicated growth processes, displaying nucleation of $PbSO_4$ films (blue) on preexisting barite steps (green), and their propagation across the surface until all terraces are covered with a strained epitaxial monolayer of $PbSO_4$.

When the surface was exposed to a lead-containing solution (9 µM $Pb(NO_3)_2$ + 100 mM H_2SO_4), we observed thin (sub-nanometer) films nucleating from all existing step edges and rapidly propagating across the barite surface, with growth rates of roughly 100 nm/min (Fig. 1a). The film is likely a (Pb,Ba)SO_4 solid solution, with trace amounts of Ba being provided by dissolution of

the sparingly soluble barite substrate. Because film growth was only observed in the lead-containing solutions, which are highly enriched in Pb^{2+} relative to Ba^{2+}, the film is presumably highly enriched in lead too, and it is hereafter referred to as a $PbSO_4$ film for brevity. The compositional difference between the original $BaSO_4$-terminated surface and the freshly grown $PbSO_4$ film is supported by the AFM phase-shift images (Fig. 1b), which show a clear contrast between the freshly grown surface and the original barite surface that is indicative of a compositional difference. Notably, the $PbSO_4$ films stopped advancing once they reached a subsequent step and would not propagate over an existing $PbSO_4$ layer to form multilayers. Thus, the surface converges toward a final condition where it is uniformly covered by a single monolayer of $PbSO_4$ and the original topography is recovered, a phenomena that was previously observed for $SrSO_4$ on barite[31]. However, the monolayer propagated slowly enough that it was possible to obtain high-resolution images of the $PbSO_4$-terminated and $BaSO_4$-terminated terraces sitting side-by-side (Fig. 1c). Crystallographic resolution was attained on both surfaces, to reveal a rectangular lattice with periodicities of ~9 Å and ~5 Å that are consistent with barite's d_{100} = 8.888 Å and d_{010} = 5.46 Å periodicities (Fig. 1e). Notably, the lattice parameters and orientations of $PbSO_4$-terminated regions are indistinguishable from those on the $BaSO_4$-terminated region, indicating that the $PbSO_4$ layer has been stretched to be commensurate with the underling $BaSO_4$ crystals (addition images are provided in SI Section 5). The corresponding lattice parameters for unstrained $PbSO_4$ are 4.5% and 1.1% smaller, a relative difference that would be clearly distinguishable in side-by-side AFM imaging if it existed (See SI Section 4). The freshly grown $PbSO_4$ films are also detectably thinner than the neighboring barite surfaces by approximately 0.20 Å (Fig. 1d). This difference is near the limit of AFM's vertical sensitivity, but it is consistent with the smaller lattice parameters of $PbSO_4$ (d_{002} = 3.58 Å for barite, the corresponding value for anglesite is 3.48 Å),

especially when we consider that the $PbSO_4$ thickness may be slightly reduced from its bulk value due to epitaxial strain.

The observed pattern of 2D film growth is distinct from previous studies of Pb-sorption on barite, which were conducted in BSS at near neutral pH instead of sulfuric acid.[12,] Instead of rapid epitaxial film growth, these studies observed the gradual incorporation of lead into the barite surface by exchange with barium. It is notable that we observed $PbSO_4$ films growing from 9 μM Pb^{2+} solutions that are undersaturated with respect to bulk $PbSO_4$. The growth of 2D $PbSO_4$ on barite from undersaturated $PbSO_4$ solutions was first observed by Murdaugh et al.[32] We have performed Visual MINTEQ calculations[33] to confirm that our 9 μM Pb^{2+} solutions are undersaturated, and calculated that the solubility limit of Pb^{2+} in 100 mM H_2SO_4 is significantly higher, at ~16 μM (see SI section 11). We have also observed micron scale anglesite particles actively dissolving in the 9 μM $Pb(NO_3)_2$ + 100 mM H_2SO_4 solutions, further demonstrating that the solutions are subsaturated with respect to $PbSO_4$. Thus, the $PbSO_4$ monolayer can be considered a surface-stabilized 2D phase.

3.2. Structure and Composition of the Film.

In situ high resolution XR data (Fig. 2a) were collected to determine structural changes at the barite (001)–water interface with varying solution compositions, i.e., from BSS to 100 mM H_2SO_4 without Pb and then with 9 μM $Pb(NO_3)_2$. These data are also shown after their normalization to the generic CTR shape (=$1/[Q^2\sin(Qd/2)^2]$. This normalization effectively reduces the intensity contribution from the bulk barite crystal, thereby enhancing the visibility of small intensity changes associated with changes in interfacial structure (Fig. 2a). Comparison of the XR and normalized XR data between BSS and the Pb-free H_2SO_4 solution shows intensity changes mostly in the Q ranges away from any of the Bragg reflections (referred to as midzones). This decrease in

midzone intensity is partly due to a slight roughening of the surface, e.g., by a decreased atomic occupancy in the topmost barite layer, driven by partial dissolution into dilute sulfuric acid. The intensity change is small, however, which is consistent with the expectation of limited dissolution (e.g., ~0.02 monolayer). More dramatic changes in XR were observed after transitioning from Pb-free solution to 9 μM $Pb(NO)_3$ H_2SO_4. Significant increases in intensity in the first midzone (i.e., Q = 0.1–1.8 $Å^{-1}$) can be attributed to an increased electron density contrast at the barite–water interface. Because the density of the solution was essentially invariant, the change is presumably due to an increase of the top solid layer density. For example, the top solid layer becomes more electron dense either when the surface is covered with higher-density (Pb-rich) films or when the Ba ions in the top barite layer are substituted by heavier Pb ions.

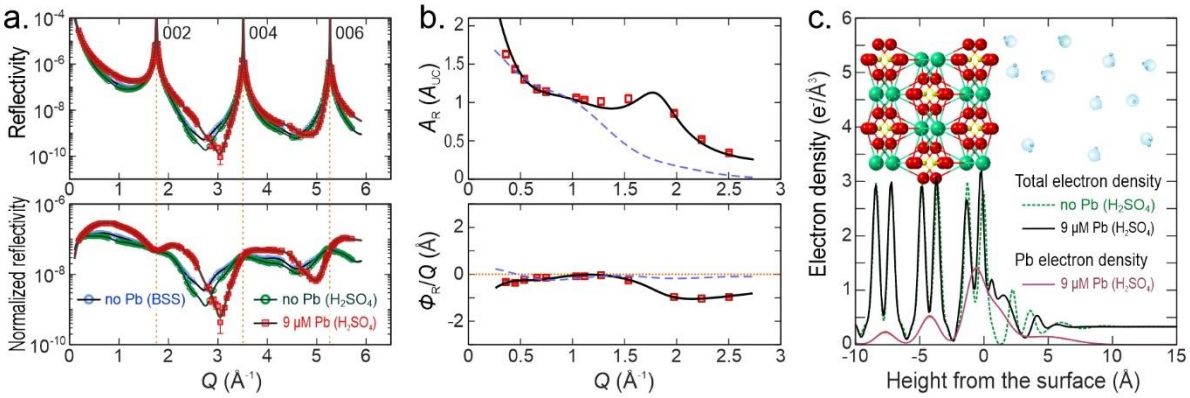

Fig 2: **a.** CTR curves comparing X-ray reflectivity of the barite (001) surface in barite-saturated solution, and in 100 mM H_2SO_4 solutions without and with 9 uM Pb, showing distinct changes in surface structure upon exposure to lead. **b.** Partial structure factor amplitude (A_R) and phase (Φ_R) of the interfacial Pb obtained from RAXR data analysis (see SI for detailed description of the analysis). The structure factor calculations from the models for the top-monolayer vs. multilayer Pb incorporation are shown in dashed blue and solid black curves, respectively. The short-dashed horizontal red line indicates the height (z = 0) of the top barite surface. **c.** electron density profiles at the barite (001)–H_2SO_4 solution interfaces in the absence and presence of 9 μM Pb (solid black and short-dashed green curves, respectively). The electron-density profile of Pb in the Pb–H_2SO_4 system is shown in solid red. The top schematic represents the barite–solution interface structure. Barium, sulfur, and oxygen atoms in the barite structure is shown as green, yellow, and red spheres, respectively. The water molecules are shown as blue spheres.

The XR data were fit to a structural model to visualize changes in the total electron-density profiles at the barite–H_2SO_4 solution interfaces (see SI Section 6 for the profile in BSS). The electron density of barite (i.e., height (z) ≤ 0 Å) is characterized by a distinct doublet pattern that corresponds to two atomic planes of heavy element Ba in each monolayer. In the absence of Pb, the solution profile has two well-defined peaks at ~2 and ~3.5 Å, which correspond to water molecules adsorbed to terminal ions Ba and SO_4 at the surface, respectively.[21] These primary hydration layers are followed by a diffuse solution peak at ~6 Å, above which the solution profile is generally featureless. In the presence of Pb, a significant increase in the top surface Ba (i.e., at $z \approx 0$ Å) is observed, which can result from exchange of Ba by heavier Pb atoms[12]. At the same time, the electron density of the solution at z between 0 and 2 Å increased significantly, which can be associated with sorption of Pb. The profile also shows slight distortions in primary hydration layers presumably due to sorption of Pb at the interface.

Element-specific RAXR data (see the spectra in SI) and corresponding model-independent analyses (Fig. 2b) provide a semiquantitative assessment of the distribution of Pb at the interface. The partial structure factor amplitude for interfacial Pb, A_{Pb}, at the lowest Q (=0.36 Å^{-1}) is ~1.5 Pb/A_{UC} and corresponds to the lowest limit of the Pb coverage at the interface.[34] ($A_{UC} = 48.4$ Å^2 is the unit cell area of the barite surface). From the partial structure factor phase, Φ_R/Q, we determine the average height of interfacial Pb is ~1 Å below the top solid surface. This indicates that most Pb uptake occurred in the solid. The Φ_R/Q values show a gradual but significant Q-dependent variation, which indicates that there are multiple Pb species sorbed at various heights (and depths) across the interface.

The RAXR data were analyzed using a structural model to quantitatively describe atomistic details of the sorbed Pb distribution at the interface (Fig. 2c). The best-fit model (χ^2 = 1.2 and R-

factor = 0.8%) consists of a series of Pb incorporated in the barite structure as well as Pb species adsorbed above the surface. The incorporated Pb has the maximum Pb coverage of ~1.2 Pb/A_{UC} in the top barite layer, which decreases with increasing depth in the subsequent layers. Structural models without this extended depth distribution for Pb yielded substantially unsatisfactory fits to the data. The depth-dependent variation in incorporated Pb coverage is expressed with an exponential decay function having its decay length of ~6 Å (SI Table S1). The layer spacing between the incorporated Pb was 3.45 ± 0.02 Å, which is shorter by ~4% than the monolayer thickness (= $d/2 \approx 3.58$ Å) of barite (001). The best-fit model also has two Pb species at z = ~1 Å and ~6 Å, having the coverages of ~0.9 Pb/A_{UC} and ~0.2 Pb/A_{UC}, respectively. These two species are interpreted as adsorbed species based on their heights with respect to the surface. Including both incorporated and adsorbed species, the total coverage of Pb is ~4 Pb/A_{UC}, exceeding the coverage expected for a monolayer overgrowth (i.e., as high as 2 Pb/A_{UC}). This large coverage as well as the wide height (and depth) distribution of interfacial Pb shows that Pb uptake at the barite (001) surface progresses by multiple processes, which likely include a Pb-rich sulfate surface monolayer as observed by AFM, buried sulfate layers with Pb-incorporation decreasing with depth, and surface-adsorbed Pb^{2+} ions.

3.3. Cyclic Exposure to Lead.

Additional in situ AFM studies investigated how barite responds to an alternating sequence of lead free 100 mM H_2SO_4 and lead rich 100 mM H_2SO_4 + 9 μM $Pb(NO_3)_2$ solutions. Each exposure lasted between three and five minutes at constant flow rates of 0.1 mL/min, with short pauses between exposures to reconfigure the perfusion system. At this flow rate, solution exchange takes approximately one minute. As described in Section 3.1, the first exposure to lead shows rapid overgrowth of a continuous lead film (Fig. 3a). In this case the growth rate was ~ 300 nm/min.

After exchanging to lead-free 100 mM H_2SO_4, holes nucleated across the dissolving film (Fig. 3b). The holes preferentially nucleated in the most recently grown regions of film, indicating that the earlier-grown regions were more stable. However, the dissolution rate decreased over time, despite a continuous flow of solution. After several minutes, this left the surface covered with a network of elongated, recalcitrant islands. High resolution imaging (Fig. 3d) shows that the retained islands possess the height and lattice structure that are characteristic of a $PbSO_4$ film, but their chemical composition as Pb-rich or Ba-rich cannot be determined. The sharp AFM-phase contrast that previously allowed us to distinguish Pb- and Ba-rich surface terminations was lost, suggesting that both the residual islands and exposed barite surfaces now possess mixed composition. Since the $BaSO_4$ surface is more resistant to dissolution than the $PbSO_4$ overgrowth, it is likely that Ba incorporation contributes to the persistence of these islands.

When the sample was re-exposed to Pb-containing solution, the film regrew with noticeably different dynamics (Fig 3c). The film nucleated from the residual islands in addition to the initial barite steps, but the overall growth rate (now ~20 nm/min) was reduced by an order of magnitude, so that the film retained some gaps even after over seven minutes of exposure. Because the growth solution and flow conditions are identical to those used in the first exposure, this indicates that the substrate itself has become less amenable to film growth. Presumably, the persistent holes in the film reflect regions of the barite surface that were especially affected. The cyclic exposure was repeated four more times, and on each exposure the regrowth of the film became slower (growth rates were reduced to ~ 8 nm/min by the 4^{th} exposure). Moreover, the surface topology became increasingly stable: the swings in coverage became smaller and the recalcitrant islands remain persistent. The likely explanation is Pb/Ba exchange has created surfaces of intermediate composition and reduced reactivity.

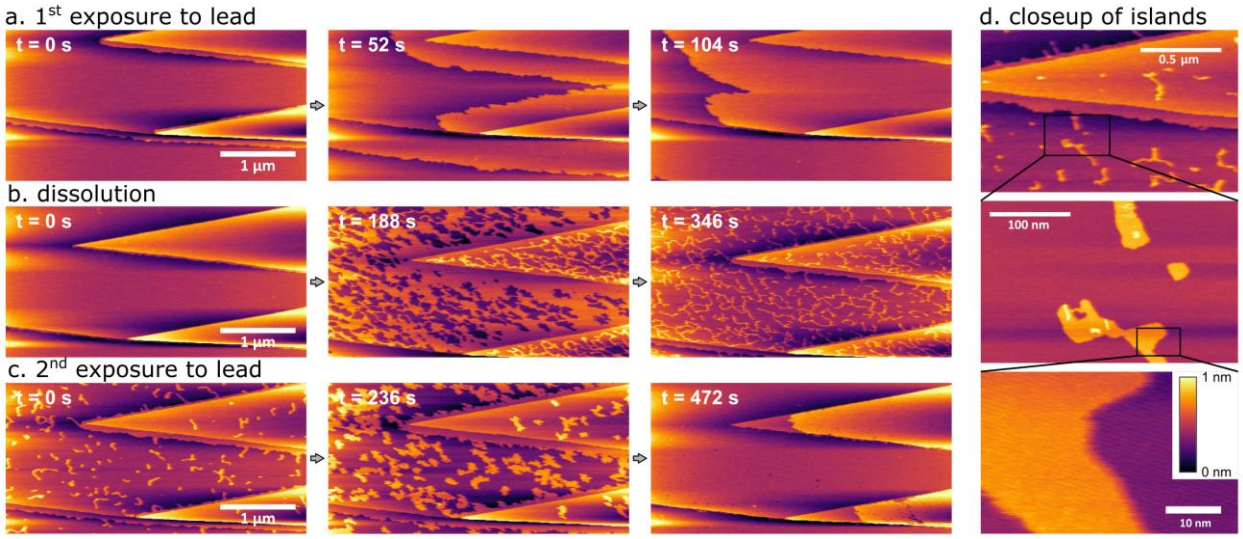

Fig. 3: AFM images of barite on cyclic lead exposure. a. AFM image sequence from first 104 seconds of first exposure to 9 µM lead in 100 mM H_2SO_4 shows the rapid growth of a continuous film, nucleating from barite step edges. **b.** AFM image sequence of same surface after subsequent 346 second exposure to lead-free 100 mM H_2SO_4, shows holes nucleating across the $PbSO_4$ film, and leaving behind slowly dissolving islands **c.** AFM image sequence after reexposure to lead causes regrowth of a $PbSO_4$ film, which nucleates from both steps and residual islands, but grows slower and remains discontinuous after 472 seconds. **d.** closeup views of the residual islands after dissolution sequence from b confirms they are flat and crystalline and retain an epitaxial match.

3.4. Refreshing surface with nitric acid.

After five cycles of exposure, we confirmed that the Pb-exposed surfaces had been altered by etching in situ with 100 mM nitric acid. The surface began with a pattern of residual islands (Fig 4a), but after six minutes of exposure to nitric acid, the islands had completely dissolved and the original barite steps had retreated by several hundred nanometers (Fig 4b). This exposed fresh barite surfaces that had never been directly exposed to lead. Next, we reintroduced a 9 µM Pb-containing sulfuric acid solution. This caused rapid film growth over the freshly exposed surface, as was observed for freshly-cleaved barite, but the growth-front slowed dramatically once it reached regions that had previously been exposed to lead. This demonstrated clearly that previous lead exposure had altered the ability of the surface to host future $PbSO_4$ films. Moreover, where

the film did advance, it preferentially regrew over the areas that had previously been covered by recalcitrant islands, demonstrating that these islands were associated with heterogeneities of the barite surface that favored island growth. Cause and effect were presumably linked here. The islands may have initially formed because they lay over barium-rich regions of the surface, but once formed, the islands would protect the underlying substrate from future lead exposure and preserve its ability to support film-growth.

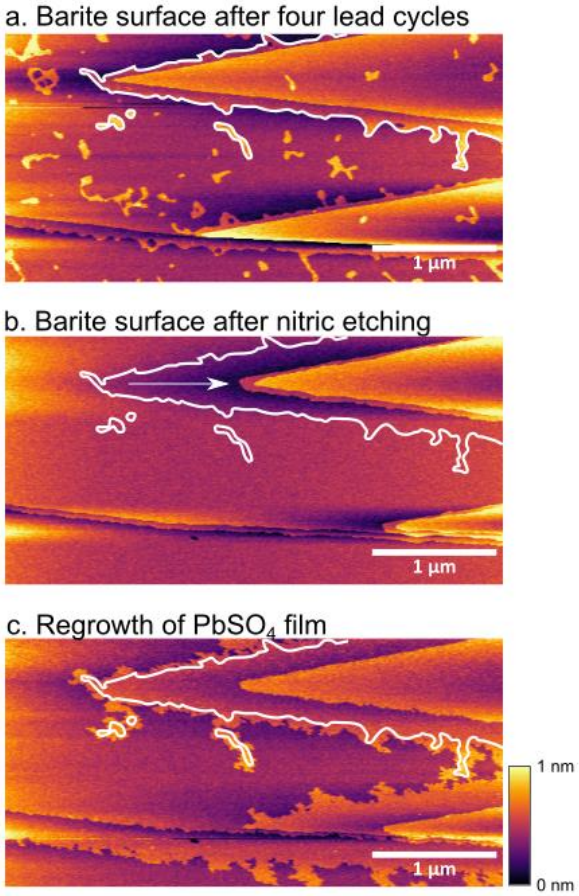

Fig. 4: Exposing a fresh barite surface with nitric acid a. AFM image of the barite (001) surface after four cyclic exposures to lead solution and lead-free H_2SO_4, showing retained islands. Selected step edges are outlined in white, to enable easier comparison to subsequent subfigures. **b**. AFM image after ~6 min exposure to 100 mM nitric acid, which removed retained islands and caused retreat of barite steps to expose fresh barite surface **c.** Image of the barite surface after reexposure to 9 uM Pb - 100 mM H_2SO_4 solution shows regrowth of a $PbSO_4$ film. The film grew rapidly across the freshly exposed barite surface, but its advancement slowed when it reached surfaces that were previously exposed to Pb.

3.5. Mechanism of Lead Incorporation.

The irreversibility of film growth after cyclic exposure to lead-containing H_2SO_4 solution is presumably related to Pb-incorporation into the topmost layers of barite. An additional experiment was performed to clarify whether Pb was incorporated via direct exchange with solution or whether the exchange was driven by $PbSO_4$ film overgrowth. We exposed a fresh-cleaved barite surface to a 100 mM H_2SO_4 solution that contained 6 μM $Pb(NO_3)_2$, until a $PbSO_4$ monolayer was grown over just part of the visible surface (SI Figure S11a). (The lower Pb^{2+} concentration was used to decrease the growth rate, making it easier to obtain a partial coverage state.) We then flushed the surface with Pb-free 100 mM H_2SO_4 to gently dissolve away the $PbSO_4$ monolayer, which left a few recalcitrant islands as before (SI Figure S11b). This created a surface where some regions had supported $PbSO_4$ for various lengths of time, and other regions never experienced $PbSO_4$ overgrowth. After reintroducing lead, we found that regrowth of the $PbSO_4$ film occurred more rapidly over the regions where the $PbSO_4$ had previously formed (SI Figure S11c), and propagation into the regions that had never experienced $PbSO_4$ overgrowth was slower (SI Figure S11d). Assuming that the reduced growth rate is a signature of increased lead incorporation, our interpretation is that more Pb was incorporated into regions that never hosted films, indicating that lead was incorporated by direct exchange from solution. When films form, they appear to cap the surface and limit further Pb-incorporation into underlying layers. Thus, the multiple layers of incorporated lead seen by RAXR can be understood as a kinetically determined state involving exchange followed by overgrowth. This is consistent with recent studies on the interaction of Pb-selenate solutions with barite, which also showed a combination of direct exchange and overgrowth.[18] Some additional mechanism would be needed to understand the apparent lead incorporation into deeper layers, i.e. the 3rd monolayer and below, albeit in a small quantity

compared to the top two monolayers. For example, it is possible that the apparent Pb incorporation in deeper layers may reflect Pb sorbed into negative topographic features of the barite surface, such as etch pits or cleavage-topography.

3.6 Absence of multilayer growth at higher lead concentrations.

To this point, the AFM experiments have only displayed monolayer growth and we have not observed multilayer formation or 3D crystal growth. Because multilayer growth is essential to 3D nucleation, we test whether multilayers may be generated by increasing $PbSO_4$ saturation. A sequence of 100 mM H_2SO_4 solutions were prepared with $[Pb]_{tot}$ ranging from 9 μM to 360 μM. At Pb concentrations of 90 μM and higher, we observed by optical microscopy that $PbSO_4$ crystals readily nucleated in solution and deposited onto the surface (SI Figure S12). Some nucleation of 3D crystals may also have occurred on macroscopic defects. However, the (001) terrace regions tracked by AFM show no evidence for multilayer formation, even in the most highly supersaturated conditions (SI Figure S13). Thus, we find that the (001) surface is remarkably ineffectual at hosting multilayer growth of $PbSO_4$.

3.7. Interpretation and Modeling.

Our results point to a barite surface that has a complex and dynamically evolving reactivity with lead. To understand this behavior we extend a thin-film growth model that Stuckenberg et al.[14] developed to understand S-K growth of pure hashemite ($BaCrO_4$) films on barite. Their thin-film model is based on two basic concepts. First, they propose that formation of a 2D wetting monolayer can be driven by surface-tension differences which favor replacing a high energy substrate-liquid interface with a lower energy film-liquid interface. This is consistent with our observation of 2D film formation, and literature suggesting that the surface tension of $PbSO_4$ is lower than that of $BaSO_4$[35]. Second, they predict that epitaxial strain energy will inhibit the formation of multilayers.

This is also consistent with our observations, as we find that multilayer growth is almost entirely suppressed. However, their model was not optimized to treat $PbSO_4$ films, nor did it consider the potential formation of mixed films. Thus, we will begin by modifying their thin-film model to consider $PbSO_4$ films and then extend it to consider films of mixed composition.

3.7.1. Pure $PbSO_4$ films.

The previous discussion described how surface tension and strain energies influence thin-film growth modes in a qualitative sense. Stuckenberg et al. defined the influence quantitatively by postulating that growth of an epitaxial film involves replacing a substrate-liquid interface (characterized by the substrate-solution interfacial tension, $\gamma_{\mathrm{BaSO_4}}$), with a film-substrate interface (characterized by $\gamma_{\mathrm{PbSO_4/BaSO_4}}$) and a strained film-solution interface (characterized by $\gamma^*_{\mathrm{PbSO_4}}$, where the * distinguishes the strained interfacial tension from that of an unstrained $PbSO_4$-solution interface). Furthermore, because the epitaxial film is strained, it has a strain energy density of U (per unit area). Thus, their model describes the excess driving force required to grow a $PbSO_4$ monolayer as $A_{UC}(U + \gamma^*_{\mathrm{PbSO_4}} + \gamma_{\mathrm{PbSO_4/BaSO_4}} - \gamma_{\mathrm{BaSO_4}})/2$, relative to growing bulk $PbSO_4$. Once the first monolayer is grown, the excess driving required to grow a second monolayer would be simply $A_{UC}U/2$.

However, the input values are not known *a priori* and can only be roughly estimated. Shutckenberg et al.[14] estimated the strain energy density of epitaxial films on barite (001) with a continuum-mechanical approximation, similar to Eq. 1.

$$U_{nom} = \frac{t}{2}\left[\varepsilon_1^2\left(c_{11} - \frac{c_{13}^2}{c_{33}}\right) + 2\,\varepsilon_1\varepsilon_2\left(c_{12} - \frac{c_{13}c_{23}}{c_{33}}\right) + \varepsilon_{22}^2\left(c_{22} - \frac{c_{23}^2}{c_{33}}\right)\right] \qquad \text{Eq. 1}$$

Here, U_{nom} denotes the nominal strain energy density, t is the film thickness, ε_i are the lattice mismatches between film and substrate, and c_{ij} are the elastic stiffness tensor elements of the film. The stiffness tensor for anglesite is not readily available, but its known elastic properties are similar

to barite[36,37], which has been extensively studied.[38, 39] By substituting barite's stiffness tensor from Ref [39], we estimate the strain energy of a $PbSO_4$ monolayer on $BaSO_4$ at $U_{nom}^{PbSO_4/BaSO_4} = 36\,\frac{\mathrm{mJ}}{\mathrm{m^2}}$ (corresponding to a strain energy density of 5.3 kJ/mol) (See SI Section 10). To estimate the substrate-solution and film-solution interfacial energies, Shtuckenberg[14] referred to the experimentally-determined values of Nielsen and Söhnel.[35] For our system, this reference provides $\gamma_{\mathrm{BaSO_4}} = 135\ \mathrm{mJ/m^2}$ and $\gamma_{\mathrm{PbSO_4}} = 100\ \mathrm{mJ/m^2}$ (note that these values are attained from nucleation-rate data, and do not consider how surface tension varies with crystal face, strain, and solution chemistry). Values for $\gamma_{\mathrm{PbSO_4/BaSO_4}}$ or $\gamma^*_{\mathrm{PbSO_4}}$ are not readily available. However, we expect that $\gamma_{\mathrm{PbSO_4/BaSO_4}}$ is low, based on the premise that chemically similar materials that form ideal solid solutions should also possess low interfacial energies. Although the thermodynamics $PbSO_4$-$BaSO_4$ solid solutions remain poorly understood, the solubility of $PbSO_4$ in $BaSO_4$ is high (estimates range from 10% up to continuous solid[40-42,43]), and calculations indicate that Ba and Pb have low pairwise interaction energies that produce a nearly-ideal solution[44].

Based on the above assumptions, we can estimate $U + \gamma^*_{\mathrm{PbSO_4}} + \gamma_{\mathrm{PbSO_4/BaSO_4}} - \gamma_{\mathrm{BaSO_4}} \approx 1\ \mathrm{mJ/m^2}$, making the excess energy to grow at just ~0.002 eV/$PbSO_4$. In contrast, the excess energy to grow the second monolayer would be 36 mJ/m^2, or ~ 0.05 eV/$PbSO_4$. This is consistent with the observation that multilayers are more difficult to grow than the first monolayer, but it is not sufficient to explain the formation of $PbSO_4$ monolayers from subsaturated solutions. Of course, this result is only an estimate and actual behavior may be more complex. For example, Shtukenberg et al. discussed the idea that strain energies could be significantly relaxed in the first monolayers, thus stabilizing the first monolayer and fostering more complex behavior for multilayers.

As a complementary approach to understand the film energetics, we performed a series of DFT simulations (See SI Section 7). The DFT simulations of strained bulk anglesite revealed $U_{nom} = 40.4\ \mathrm{mJ/m^2}$, in good agreement with estimates from Eq. 1. Moreover, simulations of barite (001) and anglesite (001) surfaces gave $\gamma_{\mathrm{BaSO_4}} = 114\ \mathrm{mJ/m^2}$ and $\gamma_{\mathrm{PbSO_4}} = 96\ \mathrm{mJ/m^2}$. Considering that the DFT calculations are zero-temperature simulations with implicit solvent, this is a remarkably close agreement with literature values. Importantly, both simulation and literature predict $\gamma_{\mathrm{PbSO_4}} < \gamma_{\mathrm{BaSO_4}}$, which would largely offset the strain energy of growing an epitaxial $PbSO_4$ monolayer. However, DFT-based calculations of $\gamma^*_{\mathrm{PbSO_4}}$ and $\gamma_{\mathrm{PbSO_4/BaSO_4}}$ paint a more complex picture, as they give $\gamma^*_{\mathrm{PbSO_4}} = 215\ \mathrm{mJ/m^2}$ (pointing to a surface energy that is highly strain-defendant), and $\gamma_{\mathrm{PbSO_4/BaSO_4}} = 124\ \mathrm{mJ/m^2}$ (which is not negligibly small). If these values are included in the thin-film model, one would predict an excess of 265 mJ/m^2 (0.4 eV/$PbSO_4$) is needed to grow the first monolayer, significantly higher than the 40 mJ/m^2 (0.06/$PbSO_4$) predicted for the second layer. This result is in stark contrast with experiment, where the first monolayer is clearly more stable than the second. To bring clarity to this, we directly calculated the excess energy of growing one-monolayer and two-monolayer films with DFT. These led to a more moderate value of 140 mJ/m^2 (0.11 eV/$PbSO_4$) for the excess driving force to grow the first monolayer, and a strikingly high 1240 mJ/m^2 (0.97 eV/$PbSO_4$) for the second monolayer, which would make second-layer growth virtually impossible. Although it still does not explain the formation of films in subsaturated conditions, this result is in closer agreement with experimentally observed suppression of multilayer films. The markedly different film-energies determined from DFT-informed model predictions and direct DFT calculations suggest that direct application of the thin-film model may not be sufficient to treat multilayer film growth in this system (the DFT-predicted energy required to grow the second layer is far higher than would be estimated from

simple epitaxial strain arguments). Thus, the films seem to display complex thickness-dependent energetics that resist a simple decomposition into strain and surface-tension terms. The physical drivers for these thickness-dependent energetics are likely a complex combination of structural and electronic relaxations that are beyond the scope of this study and will require further investigation. However, it remains possible that the thin-film model might be applied in a more limited sense by introducing corrections, such as the thickness-dependent strain relaxations invoked by Shtuckenberg.

3.7.2. Mixed (Ba,Pb) SO_4 films.

Despite questions about the detailed application of the thin-film energetic model, it still provides an important foundation for understanding films of mixed cation content. Because it resolves film-energetics into separate surface-tension and strain energy terms, and because we can reasonably predict how each term varies with film composition, we can logically extend the model to predict the energetic properties of mixed films.

For example, the strain energy of an epitaxial film is parabolic in the lattice mismatch between bulk (which defines the lattice) and film (which stretches to accommodate the mismatch). For films of mixed composition, we may approximate the lattice parameters by linear interpolation from the pure-endmembers following Vergard's law (which holds with minor deviations for bulk (Ba,Pb)SO_4 solid solutions[41]). Thus, when growing a film of fractional $PbSO_4$-composition x_i on a substrate of bulk composition x_b, we propose the assumption $U_i = (x_i - x_b)^2 U^{PbSO_4/BaSO_4}$, which simplifies to $U_i = {x_i}^2 U^{PbSO_4/BaSO_4}$ if the substrate is pure barite.

For the surface tensions of terminating surfaces, we can assume that the energy is determined by the fraction of Pb and Ba atoms exposed to solution. Thus, if x_0 is the composition of the terminating surface, we may estimate $\gamma_{x_0} = x_0\gamma_{\mathrm{PbSO_4}} + (1 - x_0)\gamma_{\mathrm{BaSO_4}}$ by linear interpolation.

Similarly, for the interfacial tension between two neighboring layers i and j, we assume that the energy is proportional to the number of Pb atoms that are 'mismatched' with Ba atoms in the adjacent layer. If Pb and Ba are distributed randomly within a layer, we would then estimate $\gamma_{i/j} = \left(x_i(1-x_j) + (1-x_i)x_j\right)\gamma_{\mathrm{PbSO_4/BaSO_4}}$.

We next consider how entropy favors the formation of mixed-composition layers by introducing the standard entropic term of an ideal solid solution, $k_bT[x\ln(x) + (1-x)\ln(1-x)]$, where k_bT is the thermal energy of 2.479 kJ/mol. (We limit ourselves to an ideal-solution model, since the excess free energy of mixing for (Pb,Ba)SO_4 solid solutions are among the lowest for sulfate solid solutions.[45,40]) Moreover, the excess free energy of mixing is largely driven by lattice strain, which can be relaxed near surfaces.

Finally, we must consider that surface energetics are linked to composition of the overlying solution. For example, lead-enriched surfaces will be more favorable when they are in contact with a lead-rich aqueous solution. We account for this in our model by incorporating a term that depends on surface composition and solution saturation with respect to bulk $PbSO_4$ and $BaSO_4$, namely, $\sigma_{PbSO_4} = \ln\{\mathrm{Pb^{2+}}\}\{\mathrm{SO_4^{2-}}\}/K_{sp}^{PbSO_4}$ and $\sigma_{BaSO_4} = \ln\{\mathrm{Ba^{2+}}\}\{\mathrm{SO_4^{2-}}\}/K_{sp}^{BaSO_4}$, where K_{sp} is the solubility product, and the brackets indicate chemical activity.

Combining the above terms and normalizing by area as appropriate, we develop a single expression to model the free energy of the surface in terms of the composition of its topmost layers. In the special case where the bulk is pure barite (*i.e.* $x_b = 0$), we obtain:

Eq. 2

$$G_{surf} = (1 - x_0)\gamma_{BaSO_4} + x_0\gamma_{PbSO_4}$$
$$+ \sum_{i \leq 0} \Big[(x_i(1 - x_{i-1}) + (1 - x_i)x_{i-1})\gamma_{\mathrm{PbSO_4/BaSO_4}}$$
$$- \frac{2k_bT}{A_{UC}}\left(x_i\sigma_{PbSO_4} - x_i\sigma_{BaSO_4}\right) + \frac{2k_bT}{A_{UC}}(x_i\, ln(x_i)\ + (1 - x_i)\, ln(1 - x_i))$$
$$+ U_i^{PbSO_4/BaSO_4}{x_i}^2 \Big]$$

Here, x_0 is the Pb-fraction in the terminating surface layer, and the summation is performed over near-surface layers whose composition differs significantly from bulk (were the *i* is an index assigned to layers, and its value denotes height relative to the terminating surface). The strain energy coefficient is written as U_i to denote the idea that the magnitude of strain-energy may be layer dependent.

To model Pb-incorporation into a barite surface via exchange, we make the simplifying assumption that only the topmost layer has any significant Pb-incorporation, and thus obtain the following function of x_0:

Eq. 3

$$G_{surf} = (1 - x_0)\gamma_{BaSO_4} + x_0\gamma_{PbSO_4} + x_0\gamma_{\mathrm{PbSO_4/BaSO_4}} - \frac{2k_bT}{A_{UC}}\left(x_0\sigma_{PbSO_4} - x_0\sigma_{BaSO_4}\right)$$
$$+ \frac{2k_bT}{A_{UC}}(x_0\, ln(x_0)\ + (1 - x_0)\, ln(1 - x_0)) + U_0^{PbSO_4/BaSO_4}{x_0}^2$$

This allows us to calculate the minimum-energy composition of the terminating surface and estimate how factors such as surface energy, strain, entropy, and saturation modify the driving force for Pb/Ba exchange into the topmost layer. In Fig 5 A. we plot this expression at various $PbSO_4$ supersaturations values, while assuming a fixed barite saturation of $\sigma_{\mathrm{BaSO_4}} = 0$. As a simple example, we use traditionally-estimated values of $\gamma_{\mathrm{BaSO_4}} = 135\ \mathrm{mJ/m^2}$, $\gamma^*_{\mathrm{PbSO_4}} =$

$100\,\frac{\mathrm{mJ}}{\mathrm{m}^2}$, and $U_0^{PbSO_4/BaSO_4} = 35\ \mathrm{mJ/m^2m}$, and assume $\gamma_{\mathrm{PbSO_4/BaSO_4}}$ is small. Under these assumptions, the predicted location of the energy minima varies from 25% Pb in an undersaturated $PbSO_4$ solution with $\sigma_{\mathrm{PbSO_4}}$=-2.3 to over 75% Pb in a supersaturated solution with $\sigma_{\mathrm{PbSO_4}}$ = +2.3. For the experimental solution conditions (i.e. 9 µM $Pb(NO_3)_2$ + 100 mM H_2SO_4), Visual MINTEQ[33] calculations estimate the solution saturation at $\sigma_{\mathrm{PbSO_4}} \approx -0.56$, for which the model predicts a minimum energy at $x_0 = 0.4$. Based on all the assumptions involved, these values should be treated as speculative. If $\gamma^*_{PbSO_4}$ or $\gamma_{\mathrm{PbSO_4/BaSO_4}}$ become very large (as in some the high-end DFT estimates), Pb-incorporation would be severally inhibited. However, these results demonstrate that more modest model parameters (in line with traditional estimates) are consistent with the experimentally observed direct-incorporation of Pb into the barite surface, even when the solutions are subsaturated with respect to bulk $PbSO_4$.

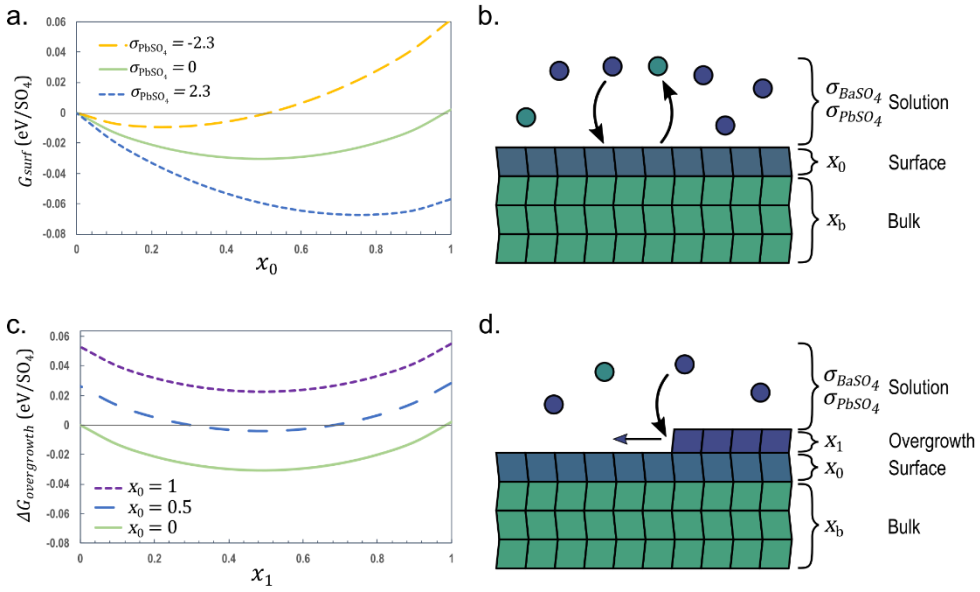

Fig. 5: Thermodynamic model of surface exchange and overgrowth based on extended thin-film model. a. Plot of surface free energy on a barite crystal vs lead-composition of the surface layer, x_0. Using model assumptions outlined in main text, calculations were performed for a pure barite substrate, assuming the solution is saturated with respect to $BaSO_4$. Three different solution saturations with respect to $PbSO_4$ are shown. All free energy curves show a minimum at intermediate composition, indicating a driving force for incorporation of lead into the barite

surface *via* exchange. **b.** Schematic of the surface exchange process, highlighting the key parameters, including composition of the solution, the surface layer, and the bulk crystal **c.** Plot of driving force for monolayer overgrowth on a barite crystal as a function of the overgrowth composition, x_s. The bulk composition, x_b, is still assumed to be 0 in all cases, but we now consider three compositions of the barite surface of $x_0 = 0$ (pristine barite), $x_0 = 0.5$ (mixed surface), $x_0 = 1$ (pure $PbSO_4$ overgrowth). In these calculations, the saturations with respect to bulk $BaSO_4$ and $PbSO_4$ are both fixed at 0. Even though neither pure $BaSO_4$ or $PbSO_4$ are favored to grow individually, the calculations predict that a mixed $PbSO_4/BaSO_4$ films can grow over a wide range of compositions. However, on a mixed surface, only intermediate compositions will grow. On a lead-terminated surface, no overgrowth of any composition will form at these saturation levels. **d.** Schematic of surface overgrowth process, highlighting the key parameters of the solution, overgrowth, underlying surface, and bulk crystal.

We now consider the driving force for growing a new layer of composition x_1 onto of a pure barite crystal ($x_b = 0$), whose terminating surface has already been altered to composition x_0. This is predicted by the following equation:

Eq. 4

$$\Delta G_{overgrowth} = (x_0 - x_1)\gamma_{Ba} + (x_1 - x_0)\gamma_{Pb} + (x_1(1 - x_0) + (1 - x_1)x_0)\gamma_{\mathrm{PbSO_4/BaSO_4}}$$
$$- \frac{2k_bT}{A_{UC}}\Big((1 - x_1)\sigma_{BaSO_4} + x_1\sigma_{PbSO_4}\Big)$$
$$- \frac{2k_bT}{A_{UC}}(x_1\, ln(x_1) + (1 - x_1)\, ln(1 - x_1)) + {x_1}^2 U_0^{PbSO_4/BaSO_4}$$

This is a simplified expression that neglects the depth dependance of strain-energy. If the strain energy is thickness dependent as suggested by Shtuckenberg, we would have to include a series of terms to account for the changing strain energy of each layer as they become more deeply buried. This expression is plotted in Fig. 5c as a function of the overgrowth composition, x_1, for three simple cases of overgrowth on a pristine barite surface ($x_0 = 0$), on a mixed surface ($x_0 = 0.5$), and on a lead-terminated film ($x_0 = 1$), using the same parameters as we used for Fig. 5a, while assuming the solutions are saturated with respect to both $PbSO_4$ and $BaSO_4$ ($i.e. \sigma_{BaSO_4} = 0$, $\sigma_{PbSO_4} = 0$).

Under the above assumptions, we find that $\Delta G_{overgrowth}$ is negative for almost all compositions, so long as the growth occurs on a pristine barite surface. This indicates that there is initially a strong driving force to overgrow a $PbSO_4$-containing film. The most thermodynamically stable film is predicted to have a mixed composition (here $x_1 \approx 0.5$), but we expect that kinetics may favor the growth of more Pb-rich films, due to the relative scarcity of Ba^{2+} ions in solution relative to Pb^{2+} ions. The surface composition would presumably relax toward its equilibrium composition later, via a slower process in which barite dissolves to allow Ba^{2+}/Pb^{2+} exchange between the film and solution.

The situation changes considerably when we consider overgrowth of films on mixed $Pb_{0.5}Ba_{0.5}SO_4$ surface termination ($x_0 = 0.5$). Now we predict that pure $PbSO_4$ films are thermodynamically inhibited from growing unless the $PbSO_4$ saturation is substantially increased, and it would only be possible to grow a film if they are stabilized by the incorporation of barium.

Finally, when we consider the overgrowth of $PbSO_4$ on an existing $PbSO_4$ surface-termination, we predict that growth of any film composition is prohibited unless the solution saturation is dramatically increased. This is consistent with the inhibition of $PbSO_4$ multilayers observed in AFM. In principle, it would be possible to grow a second layer at sufficiently high $PbSO_4$ saturations, but these saturations may not be experimentally accessible. For example, using the above model parameters, we estimate that lead-rich multilayers would require $Pb(NO_3)_2$ concentrations on the order of 70 μM or higher. Although we can prepare solutions at these concentrations, our experiments show that these solutions are unstable and are likely to rapidly precipitate bulk $PbSO_4$ crystals.

Even more complex behaviors can be attained if we consider the full range of variables, such as the substrate-film interfacial tension term ($\gamma_{PbSO_4/BaSO_4}$) or depth-dependent strain. Unfortunately,

untangling these complexities is beyond the reach of our current study. What we hope to emphasize however, is that mixed-films provide important new dimensions of complexity that have not been considered in previous models of thin-film growth from solution, and may allow mixed films to grow when traditional models suggest that growth of pure-films is inhibited.

Our model and DFT calculations highlight the potential for substantial Pb-incorporation into the barite surface, even from solutions that are subsaturated with respect to $PbSO_4$, consistent with our experimental observations by AFM and RAXR. Moreover, the calculations predict that this Pb-incorporation will substantially alter the driving force for growing subsequent layers. Thus, they provide a foundation for understanding the mechanistic interconnections between ion-exchange processes and film growth.

Another key prediction of the model is that there are conditions where the thermodynamic driving forces prohibit the growth of pure $PbSO_4$ films, but mixed films can still be achieved. This may help reconcile some experimental and theoretical results. For example, DFT calculations predicted that pure $PbSO_4$ films should not form from subsaturated solutions, which appears to conflict with the experimental observation of film-growth in subsaturated solutions. This apparent conflict could be resolved if the films are stabilized by $BaSO_4$ incorporation. As the host surface becomes richer in lead (and thus less favorable for film growth), more stabilizing barium would be needed. The need to incorporate $BaSO_4$ could have important consequences for growth rates, because the dynamics of mixed-film growth can be very different from those of pure films.

As a final note, our experiments suggest that multilayer growth is strongly inhibited, consistent with the high epitaxial strain energy for $PbSO_4$ on the barite (001) surface. However, if multilayer films were to form on barite (001), it is worth considering whether they would occur as continuous layers (F-VdM growth) or islands (S-K growth). We may gain insights here by comparing to

literature for similar systems. For example, $SrSO_4$ has a relatively low mismatch with $PbSO_4$ and shows F-VdM growth.[17] A similar growth mode was observed for $PbSeO_4$ on $BaSO_4$.[18] However, materials with higher lattice mismatches, closer to that of $PbSO_4$ on $BaSO_4$ (such as $BaCrO_4$ on $BaSO_4$[14] and $SrSO_4$ on $BaSO_4$[16]) tend to form islands. In this light, we expect that if $PbSO_4$ can be induced to form multilayers on barite, they are likely to grow via an S-K mode.

4. Conclusions

Several important findings arise from our studies. First is the discovery that barite (001) is highly effective at supporting 2D monolayer films of $PbSO_4$, even from subsaturated solutions, but it is not effective at supporting multilayer film growth or 3D nucleation. Through the lens of thin-film theories, the remarkable ability of barite (001) to host 2D epitaxial $PbSO_4$ films may be partly attributed to the wetting force to replace a pristine $BaSO_4$-terminated surface with a $PbSO_4$-terminated surface of lower surface tension. With a naïve application of classical nucleation theory, this might be expected to make barite an ideal nucleator for bulk $PbSO_4$. However, epitaxial strain appears to ultimately suppress the formation of multilayers, thus making the barite (001) surface an ineffective nucleator of bulk $PbSO_4$. In similar systems such as hashemite on barite (001), it has been possible to overcome strain energy and drive the formation of multilayers by increasing saturation. However, the estimated strain energies for hashemite on barite (001) are moderate when compared to those for anglesite on barite (001) (U_{nom} = 22 mJ/m^2 for hashemite *vs* U_{nom} = 36 mJ/m^2 for anglesite). The higher strain energy for $PbSO_4$ makes it functionally impossible to grow $PbSO_4$ multilayers on barite (001), since the highly saturated solutions required to drive epitaxial growth will be unstable and undergo rapid bulk nucleation first. Thus, we expect that a key avenue for improving barite's effectiveness as a nucleator in lead-acid batteries will be to reduce strain energies. Despite our finding that (001) is an ineffective nucleator of multilayer anglesite, there is

still significant evidence that barite crystals do facilitate anglesite nucleation.[4, 5] A likely explanation is that nucleation occurs on surfaces that present a better lattice match with anglesite, such as the (210) face. Bulk nucleation may also be favored at defects where strain can be relieved, such as fractures and large-scale step-edges. Thus, another avenue for facilitating nucleation may be to produce barite particles that express more of the faces and defects that favor nucleation. This might be achieved by tuning barite growth conditions to produce smaller sizes[10], or tailored morphologies[46].

A second important discovery is the observation of gradually varying surface cation compositions in the topmost layers. The formation of these altered layers presumably results from isomorphic substitution of Ba^{2+} in the crystal lattice by Pb^{2+} from the solution. However, the mechanism that enables the extended depth of the Pb profile into multiple barite monolayers is not fully understood. Moreover, these altered surfaces show distinctly different reactivity than pristine surfaces, so that Pb^{2+}/Ba^{2+} exchange acts in competition to 2D film overgrowth. Our results clearly show that altered surfaces are less effective at hosting 2D $PbSO_4$ films than the pristine barite surfaces. This may mean that 2D $PbSO_4$ film growth is a transient phenomenon that only occurs early in a battery's lifetime. Nevertheless, the film growth may have long-term impact. Moreover, the nucleation, growth and dissolution of 2D films during cycling leads to a time-evolving pattern of increasingly recalcitrant islands. If these prove to be long-lived topographic features, it is possible that 2D film growth during the initial exposure to acidic Pb solution could influence the subsequent reactivity of the substrate during a battery's operational lifetime.

The coupling between ion exchange and film growth can be understood phenomenologically by using our thermodynamic model for films of mixed composition, which is tested against DFT calculations. The model provides a framework for understanding the behavior of mixed films at

the barite-solution interface, and also provides rationalization for the strongly-enhanced growth of Pb-rech sulfate monolayers on pristine barite surfaces – where formation of films from subsaturated solutions may be explained as (1) surface-tension stabilized films, consistent with traditional S-K theory, or (2) entropy-stabilized films through mixture of $BaSO_4$ and $PbSO_4$. It also explains how Pb-incorporation can influence surface-tensions to suppress the formation of subsequent layers. However, significantly more work would be needed to accurately refine the model parameters in S-K growth, including systematic experiments and DFT calculations to determine precisely how strain energies and surface tension depend on film composition and thickness.

Based on our model calculations and experimental observations, we may speculate on how barite's effectiveness as a nucleator might be evaluated at the molecular level. Our models predict that Pb-incorporation into the barite surface can have significant impacts on subsequent 2D film growth, primarily through its influence on surface tensions. Despite this strong effect on 2D film growth, the influence of surface chemistry on multilayer and 3D growth is probably less pronounced. As additional layers form, epitaxial strain is probably a dominant influence (consistent with AFM measurements, which show strong epitaxy between layers). Unless strain-relieving defects can be introduced in the film (as might occur at surface defects like step-edges), one way to reduce strain energies may be to grow on surfaces with better lattice matches.

More generally, our results can provide important insights into related problems in fundamental geochemistry and crystal growth. The distinct differences between the rapid process of 2D film growth seen here (where the H_2SO_4 provides a large excess of SO_4 ions), and the slower Pb/Ba exchange processes that were observed in near-neutral barite-saturated aqueous solutions may help to elucidate how solution chemistry can determine lead sorption mechanisms. This is important

not just to batteries (for example, as H_2SO_4 concentration varies during charging and discharging), but also to geochemical problems where it is important to understand the mobility of lead and its pH-dependent sorption on surfaces (e.g., in acid mine drainage vs in industrially impacted freshwater aquifers). The basic framework of our thermodynamic model should also have a wide applicability to other systems that display heteroepitaxial growth. Considering the clear impacts of ion-exchange on film growth seen here, it would be interesting to consider whether the formation chemically mixed surfaces play a similar role in the behavior of other heteroepitaxial mineral-solution pairs.

ASSOCIATED CONTENT

Supporting Information.

The Supporting Information is available free of charge as a PDF document. This includes photographs and X-ray fluorescence spectra of the barite sample, schematics of the AFM cell, supplementary AFM images, details of XRR data analysis, details of atomistic modeling, supplementary calculations on epitaxial strain, and calculations of solution speciation.

AUTHOR INFORMATION

Corresponding Authors

*Benjamin A. Legg, benjamin.legg@pnnl.gov

*Vijayakumar Murugesan, vijay@pnnl.gov

Author Contributions

B.A. Legg, S.S. Lee, and T.T. Fister designed experiments. B.A. Legg conducted AFM measurement and analysis. S.S. Lee conducted X-ray reflectivity measurements and analysis. J. Garcia and H. Iddir conducted DFT calculations. B.A. Legg conducted thermodynamic model calculation. The manuscript was written through contributions of all authors. All authors have given approval to the final version of the manuscript.

Funding Sources

This research is funded by the DOE Office of Research and Development under the Office of Electricity "Cost-Competitive Energy Storage" project.

Acknowledgment: The authors would like to acknowledge financial support primarily from the U.S. Department of Energy's (DOE's) Office of Electricity (OE) Energy Storage program (under Contract No. 57558). The in-situ X-ray reflectivity data and fluorescence spectra were collected at beamlines 33-ID-D and 33-BM-C, respectively, at Advanced Photon Source. Use of the Advanced Photon Source was supported by the U.S. Department of Energy, Office of Science, Office of Basic Energy Sciences, under Contract DE-AC02-06CH11357 to UChicago Argonne, LLC as operator of Argonne National Laboratory.

REFERENCES

(1) Viswanathan, V.; Mongird, K.; Franks, R.; Li, X.; Sprenkle, V.; Baxter, R. *2022 Grid Energy Storage Technology Cost and Performance Assessment*; PNNL-33283; U.S. Department of Energy, 2022.
(2) Lopes, P. P.; Stamenkovic, V. R. Past, Present, and Future of Lead–Acid Batteries. *Science* **2020**, *369* (6506), 923-924.
(3) Pavlov, D. *Lead-Acid Batteries: Science and Technology*; Elsevier, 2011. Hampson, N.; Lakeman, J. Fundamentals of Lead-Acid Cells: Part Xiii. The Influence of Additives on the Charge and Discharge Processes of the Negative Electrode. *Journal of Electroanalytical Chemistry and Interfacial Electrochemistry* **1981**, *119* (1), 3-15.
(4) Pavlov, D.; Nikolov, P.; Rogachev, T. Influence of Expander Components on the Processes at the Negative Plates of Lead-Acid Cells on High-Rate Partial-State-of-Charge Cycling. Part I: Effect of Lignosulfonates and Baso4 on the Processes of Charge and Discharge of Negative Plates. *Journal of Power Sources* **2010**, *195* (14), 4435-4443.
(5) Vermesan, H.; Hirai, N.; Shiota, M.; Tanaka, T. Effect of Barium Sulfate and Strontium Sulfate on Charging and Discharging of the Negative Electrode in a Lead–Acid Battery. *Journal of power sources* **2004**, *133* (1), 52-58.
(6) Boden, D. Selection of Pre-Blended Expanders for Optimum Lead/Acid Battery Performance. *Journal of power sources* **1998**, *73* (1), 89-92.

(7) Yuan, X.; Hu, J.; Xu, J.; Hu, Y.; Zhang, W.; Dong, J.; Liang, S.; Hou, H.; Wu, X.; Yang, J. The Effect of Barium Sulfate-Doped Lead Oxide as a Positive Active Material on the Performance of Lead Acid Batteries. *Rsc Advances* **2016**, *6* (32), 27205-27212.
(8) Bode, H. Lead-Acid Batteries. **1977**.
(9) Vanýsek, P.; Bača, P.; Zimáková, J.; Vaculík, S.; Bouška, M. In-Situ Afm Observations of the Effect of Addition of Glass Fibers and Lignosulfonates on Performance of the Negative Active Mass of a Lead-Acid Storage Battery. *Journal of Energy Storage* **2020**, *29*, 101318.
(10) Hosseini, S.; Farhadi, K.; Banisaeid, S. Improving Particle Size of Baso4 with a Unique Glycerol Base Method and Its Impact on the Negative Active Material of the Lead-Acid Battery. *Journal of Energy Storage* **2019**, *21*, 139-148.
(11) Huck, M.; Sauer, D.-U. Modeling Transient Processes in Lead-Acid Batteries in the Time Domain. *Journal of Energy Storage* **2020**, *29*, 101430.
(12) Bracco, J. N.; Lee, S. S.; Braha, I.; Dorfman, A.; Fenter, P.; Stack, A. G. Pb Sorption at the Barite (001)–Water Interface. *The Journal of Physical Chemistry C* **2020**, *124* (40), 22035-22045.
(13) Turnbull, D. Kinetics of Heterogeneous Nucleation. *The Journal of Chemical Physics* **1950**, *18* (2), 198-203.
(14) Shtukenberg, A. G.; Astilleros, J. M.; Putnis, A. Nanoscale Observations of the Epitaxial Growth of Hashemite on Barite (0 0 1). *Surface Science* **2005**, *590* (2-3), 212-223.
(15) Forjanes, P.; Gómez-Barreiro, J.; Morales, J.; Astilleros, J. M.; Fernández-Díaz, L. Epitactic Growth of Celestite on Anhydrite: Substrate Induced Twinning and Morphological Evolution of Aggregates. *CrystEngComm* **2020**, *22* (35), 5743-5759.
(16) Sánchez-Pastor, N.; Pina, C. M.; Astilleros, J. M.; Fernández-Díaz, L.; Putnis, A. Epitaxial Growth of Celestite on Barite (0 0 1) Face at a Molecular Scale. *Surface science* **2005**, *581* (2-3), 225-235.
(17) Pina, C. M.; Rico-García, A. Nanoscale Anglesite Growth on the Celestite (0 0 1) Face. *Surface science* **2009**, *603* (17), 2708-2713.
(18) Yang, P.; Rampal, N.; Weber, J.; Bracco, J. N.; Fenter, P.; Stack, A. G.; Lee, S. S. Synergistic Enhancement of Lead and Selenate Uptake at the Barite (001)–Water Interface. *Environmental Science & Technology* **2022**.
(19) Bethke, C. M.; Yeakel, S. *The Geochemist's Workbench: Reference Manual*; Aqueous Solutions, LLC, 2013.
(20) Fenter, P. A. X-Ray Reflectivity as a Probe of Mineral-Fluid Interfaces: A User Guide. *Reviews in mineralogy and geochemistry* **2002**, *49* (1), 149-221.
(21) Bracco, J. N.; Lee, S. S.; Stubbs, J. E.; Eng, P. J.; Heberling, F.; Fenter, P.; Stack, A. G. Hydration Structure of the Barite (001)–Water Interface: Comparison of X-Ray Reflectivity with Molecular Dynamics Simulations. *J. Phys. Chem. C* **2017**, *121* (22), 12236-12248. DOI: 10.1021/acs.jpcc.7b02943.
(22) Kresse, G.; Furthmüller, J. Efficiency of Ab-Initio Total Energy Calculations for Metals and Semiconductors Using a Plane-Wave Basis Set. *Computational materials science* **1996**, *6* (1), 15-50.
(23) Kresse, G.; Hafner, J. Ab Initio Molecular Dynamics for Liquid Metals. *Physical review B* **1993**, *47* (1), 558.
(24) Perdew, J. P.; Burke, K.; Ernzerhof, M. Generalized Gradient Approximation Made Simple. *Physical review letters* **1996**, *77* (18), 3865.
(25) Blöchl, P. E. Projector Augmented-Wave Method. *Physical review B* **1994**, *50* (24), 17953.

(26) Mathew, K.; Kolluru, V. C.; Mula, S.; Steinmann, S. N.; Hennig, R. G. Implicit Self-Consistent Electrolyte Model in Plane-Wave Density-Functional Theory. *The Journal of Chemical Physics* **2019**, *151* (23), 234101.
(27) Mathew, K.; Sundararaman, R.; Letchworth-Weaver, K.; Arias, T.; Hennig, R. G. Implicit Solvation Model for Density-Functional Study of Nanocrystal Surfaces and Reaction Pathways. *The Journal of chemical physics* **2014**, *140* (8), 084106.
(28) Pina, C.; Bosbach, D.; Prieto, M.; Putnis, A. Microtopography of the Barite (0 0 1) Face During Growth:: Afm Observations and Pbc Theory. *Journal of crystal growth* **1998**, *187* (1), 119-125.
(29) Pina, C. M.; Becker, U.; Risthaus, P.; Bosbach, D.; Putnis, A. Molecular-Scale Mechanisms of Crystal Growth in Barite. *Nature* **1998**, *395* (6701), 483-486.
(30) Bracco, J. N.; Gooijer, Y.; Higgins, S. R. Hydrothermal Atomic Force Microscopy Observations of Barite Step Growth Rates as a Function of the Aqueous Barium-to-Sulfate Ratio. *Geochimica et Cosmochimica Acta* **2016**, *183*, 1-13.
(31) Astilleros, J. M.; Pina, C. M.; Fernández-Díaz, L.; Putnis, A. Nanoscale Growth of Solids Crystallising from Multicomponent Aqueous Solutions. *Surface Science* **2003**, *545* (1-2), L767-L773.
(32) Murdaugh, A. E.; Liddelow, M.; Schmidt, A. M.; Manne, S. Two-Dimensional Crystal Growth from Undersaturated Solutions. *Langmuir* **2007**, *23* (11), 5852-5856.
(33) Gustafsson, J. P. Visual Minteq 3.0 User Guide. *KTH, Department of Land and Water Recources, Stockholm, Sweden* **2011**.
(34) Park, C.; Fenter, P. A. Phasing of Resonant Anomalous X-Ray Reflectivity Spectra and Direct Fourier Synthesis of Element-Specific Partial Structures at Buried Interfaces. *J. Appl. Crystallogr.* **2007**, *40*, 290-301.
(35) Nielsen, A. E.; Söhnel, O. Interfacial Tensions Electrolyte Crystal-Aqueous Solution, from Nucleation Data. *Journal of Crystal Growth* **1971**, *11* (3), 233-242.
(36) Korabel'nikov, D.; Zhuravlev, Y. N. Structural, Elastic, Electronic and Vibrational Properties of a Series of Sulfates from First Principles Calculations. *Journal of Physics and Chemistry of Solids* **2018**, *119*, 114-121.
(37) Li, B.; Xu, J.; Chen, W.; Ye, Z.; Huang, S.; Fan, D.; Zhou, W.; Xie, H. Compressibility and Expansivity of Anglesite (Pbso4) Using in Situ Synchrotron X-Ray Diffraction at High-Pressure and High-Temperature Conditions. *Physics and Chemistry of Minerals* **2018**, *45* (9), 883-893.
(38) Rao, T. S. Elastic Constants of Barytes and Celestite. In *Proceedings of the Indian Academy of Sciences-Section A*, 1951; Springer: Vol. 33, pp 251-256. Haussühl, S. Elastic and Thermoelastic Properties of Isotypic Kclo4, Rbclo4, Csclo4, Tlclo4, Nh4clo4, Tlbf4, Nh4bf4 and Baso4. *Zeitschrift für Kristallographie - Crystalline Materials* **1990**, *192* (1-4), 137-146. DOI: doi:10.1524/zkri.1990.192.14.137. Becker, U.; Risthaus, P.; Brandt, F.; Bosbach, D. Thermodynamic Properties and Crystal Growth Behavior of the Hashemite (Baso4–Bacro4) Solid Solution. *Chemical geology* **2006**, *225* (3-4), 244-255.
(39) Santamaría-Pérez, D.; Kumar, R. S.; Dos Santos-Garcia, A.; Errandonea, D.; Chulia-Jordan, R.; Saez-Puche, R.; Rodríguez-Hernández, P.; Muñoz, A. High-Pressure Transition to the Post-Barite Phase in Bacro 4 Hashemite. *Physical Review B* **2012**, *86* (9), 094116.
(40) Fernández-González, A.; Carneiro, J.; Katsikopoulos, D.; Prieto, M. Thermodynamic Properties of the (Ba, Pb) So4 Solid Solution under Ambient Conditions: Implications for the Behavior of Pb and Ra in the Environment. *Geochimica et Cosmochimica Acta* **2013**, *105*, 31-43.

(41) Lee, J.-S.; Wang, H.-R.; Iizuka, Y.; Yu, S.-C. Crystal Structure and Raman Spectral Studies of Baso4—Pbso4 Solid Solution. *Zeitschrift für Kristallographie-Crystalline Materials* **2005**, *220* (1), 1-9.
(42) Kornicker, W. A.; Presta, P. A.; Paige, C. R.; Johnson, D. M.; Hileman Jr, O. E.; Snodgrass, W. J. The Aqueous Dissolution Kinetics of the Barium/Lead Sulfate Solid Solution Series at 25 and 60 C. *Geochimica et Cosmochimica Acta* **1991**, *55* (12), 3531-3541.
(43) Takano, B.; Yanagisawa, M.; Watanuki, K. Structure Gap in Baso4-Pbso4 Solid Solution Series. *Mineralogical Journal* **1970**, *6* (3), 159-171.
(44) Vinograd, V.; Kulik, D.; Brandt, F.; Klinkenberg, M.; Weber, J.; Winkler, B.; Bosbach, D. Thermodynamics of the Solid Solution-Aqueous Solution System (Ba, Sr, Ra) So4+ H2o: I. The Effect of Strontium Content on Radium Uptake by Barite. *Applied geochemistry* **2018**, *89*, 59-74.
(45) Zhu, C. Coprecipitation in the Barite Isostructural Family: 1. Binary Mixing Properties. *Geochimica et Cosmochimica Acta* **2004**, *68* (16), 3327-3337.
(46) Godinho, J. R.; Stack, A. G. Growth Kinetics and Morphology of Barite Crystals Derived from Face-Specific Growth Rates. *Crystal Growth & Design* **2015**, *15* (5), 2064-2071.

SYNOPSIS TOC

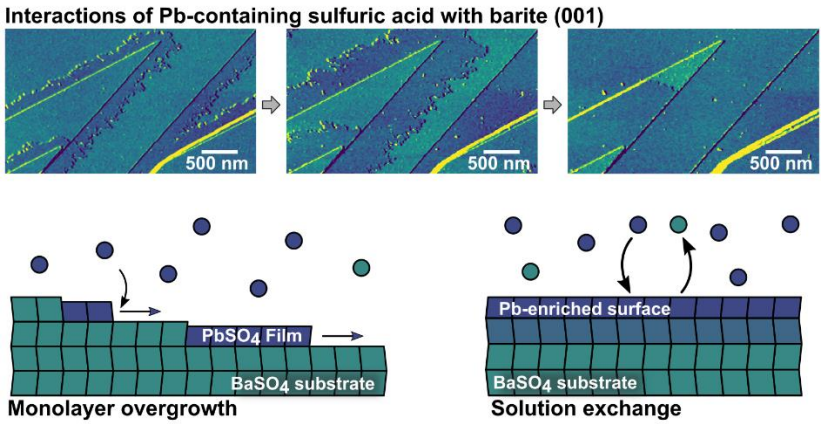

Supporting Information

Uptake of Pb and formation of mixed (Ba,Pb)SO_4 monolayers on barite during cyclic exposure to lead-containing sulfuric acid

Benjamin. A. Legg[1], Sang Soo Lee[2], Juan C. Garcia[2], Hakim Iddir[2], Tim T. Fister[2], Vijayakumar Murugesan[1*]*

1. Physical Sciences Division, Pacific Northwest National Laboratory, Richland WA, USA.
2. Chemical Sciences and Engineering Division, Argonne National Laboratory, Lemont, IL 60439 USA.

Corresponding Authors
* Benjamin A. Legg, benjamin.legg@pnnl.gov
* Vijayakumar Murugesan, vijay@pnnl.gov

Contents

1. Barite sample

The barite (001) surfaces for this study were prepared by cleaving crystals from a naturally-occurring barite geode from Sichuan, China. An image of cleaved sample, mounted for atomic force microscopy (AFM) imaging is shown in Figure S1.

Figure S1: Example image of a barite crystal. *The crystal is mounted on a 12 mm diameter AFM sample puck with Crystalbond™ 509 adhesive, with the fresh-cleaved 001 face exposed. Photo taken after experiment was complete.*

2. Barite composition.

A sample crystal from the barite geode used in this study was characterized using X-ray fluorescence spectroscopy, as show in Fig. S2. The results show that the barite purity is greater than 99.9% with respect to the cation content, with the major impurity being Sr, at a content of less than 0. 1%. (Values are in atomic percent).

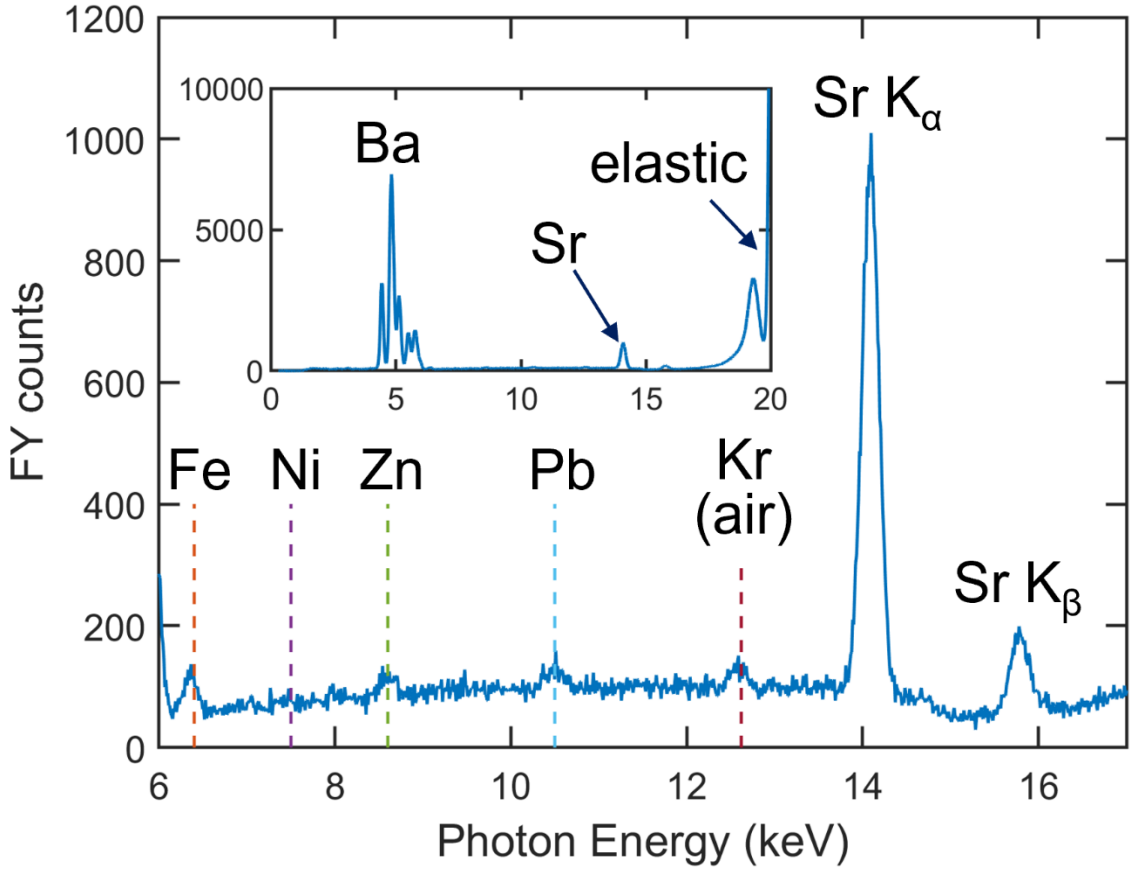

Figure S2: X-ray fluorescence spectrum of a barite crystal from the geode used in this study*. The spectrum was collected using 20 keV incident X-rays at sector 33-BM-C, Advanced Photon Source, Argonne National Laboratory. A thin layer of aluminum foil was used to reduce the Ba fluorescence signals from the bulk. The main plot displays the magnified view of the spectrum between 6 and 17 keV of photon energies. The full spectrum is shown in the inset figure. Inclusion of trace impurity elements, Fe, Ni, Zn, Pb, and Sr, of the crystal are detected in the crystal. The cation-based mole fraction of the most dominant impurity element Sr is estimated at less than 0.1atomic % with respect to Ba.*

3. AFM Perfusion Cell Schematic

AFM imaging was performed in a Cypher VRS AFM (Asylum Research, Oxford Instruments), using the commercially available perfusion cell with PTFE tubing. The operating mode utilized the PTFE tubing to exchange solutions in a small meniscus of dilute sulfuric-acid solution, as shown **Figure S3**. A push-pull syringe pump was used to maintain a constant meniscus volume during solution exchange.

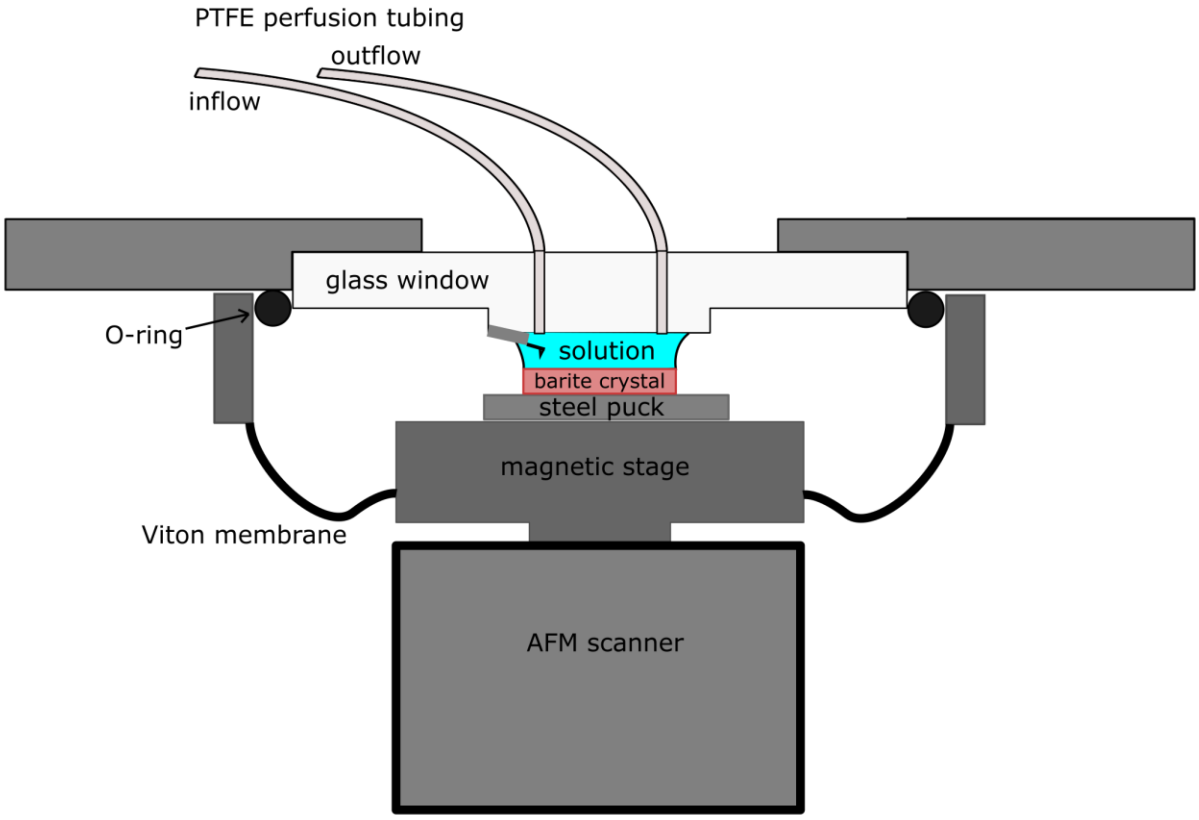

Figure S3: Schematic of AFM perfusion cell operation mode for in situ imaging. *(Schematic not to scale). The imaging is performed in a small meniscus of solution (Typically on the order of ~50 uL in volume), which is exchanged via PTFE perfusion tubing that is attached to a syringe pump. The sample chamber is enclosed with a Viton membrane, which helps protect sensitive instrumentation and limit evaporation of the sample during imaging.*

4. Measurement of Lattice Periodicities with In Situ AFM

In the main text, high resolution images were used to confirm that the surface lattice periodicities the barite surface and overgrown $PbSO_4$ film were identical. To demonstrate that high-resolution AFM imaging has the capability to image very small changes in lattice periodicity, a complementary experiment is shown in **Figure S4**, in which the lattice periodicities of a barite crystal and a nearby micron-scale anglesite crystal are compared.

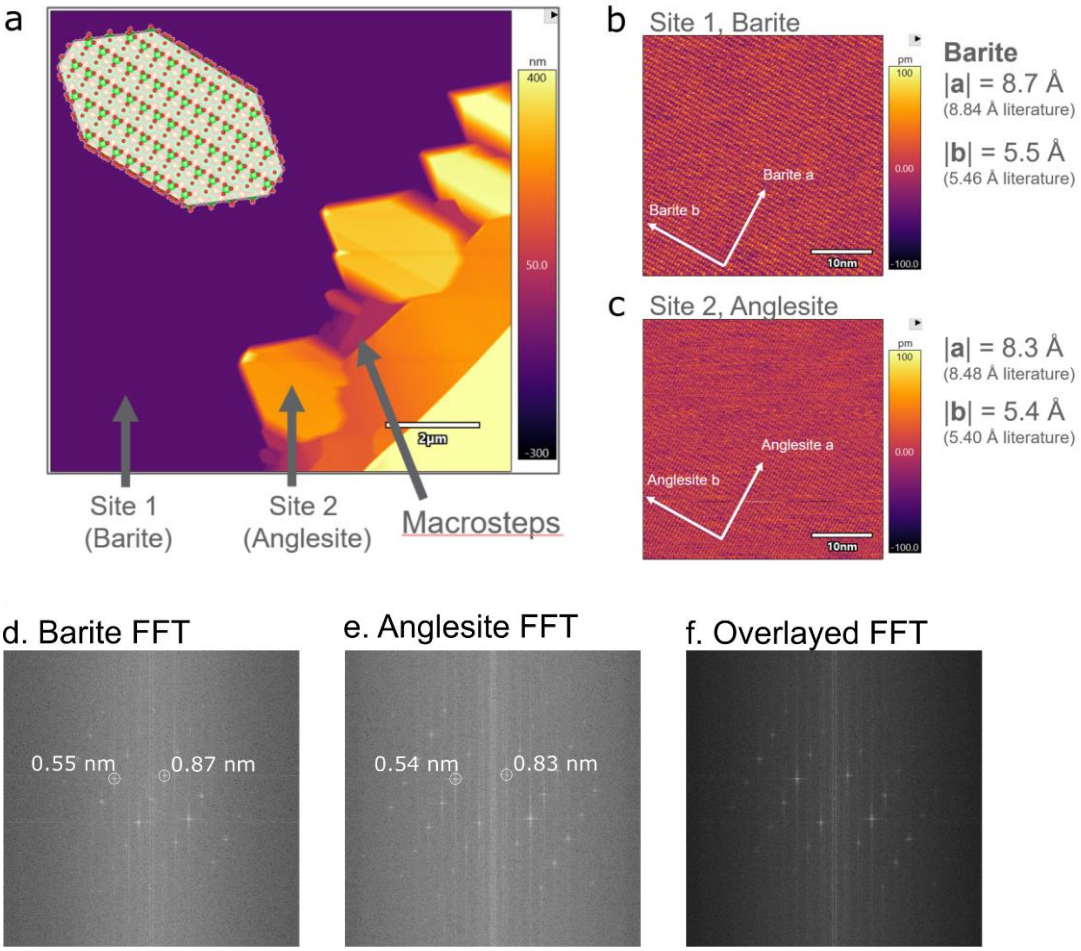

Figure S4: Demonstration of the ability to measure subtle changes in crystal lattice parameters with AFM. a. *Shows a large-scale image of a barite surface, upon which micron-scale anglesite particles have been grown. These particles did not grow directly on the (001) surface, but grew on macroscopic steps that were formed during cleavage. Due to their large size (several hundred nm tall), we expect the particle lattice parameters will be those of bulk anglesite. The inset shows a drawing of an oriented nanoscale anglesite particle to demonstrate the relationship between habit and lattice plane orientations. Two sites (Site 1 and 2) are indicated, where subsequent side-by-side high resolution images of barite (001) and anglesite (001), respectively, were obtained (for convenience, we refer to anglesite directions using the standard barite indexing scheme).* ***b.*** *Shows a lattice-resolution image of the barite (001) surface, obtained in situ, with the barite a and b lattice directions highlighted. Measured lattice parameters of ~8.7 Å and 5.5 Å are consistent with expected literature values (8.84 Å and 5.46 Å) within a 2% error.* ***c.*** *Shows an equivalent lattice-resolution image on the anglesite particle. The lattice parameters are 8.3 Å and 5.4 Å. As before, this is a few percent smaller than literature values. However, the lattice mismatches from AFM experiments are 4.6% and 0.9%, which is in good agreement with the expected mismatches of 4.3% and 1.1%. (Note that both images were obtained 'scan up' to ensure any distortions were equivalent in each image)* ***d.*** *shows an FFT of the barite image with lattice parameters marked.* ***e.*** *shows a similar FFT of the anglesite image, also with lattice parameters marked.* ***f.*** *shows an overlay of the two FFTs. The FFT's orientations are identical, but peaks are broadened (reflecting the slightly different lattice parameter obtained from each image. This demonstrates the ability to accurately detect and quantify very small (percent-scale) changes in surface lattice periodicity using side-by-side AFM imaging.*

5. High Resolution Imaging of $PbSO_4$ Monolayer and $BaSO_4$ terrace lattices.

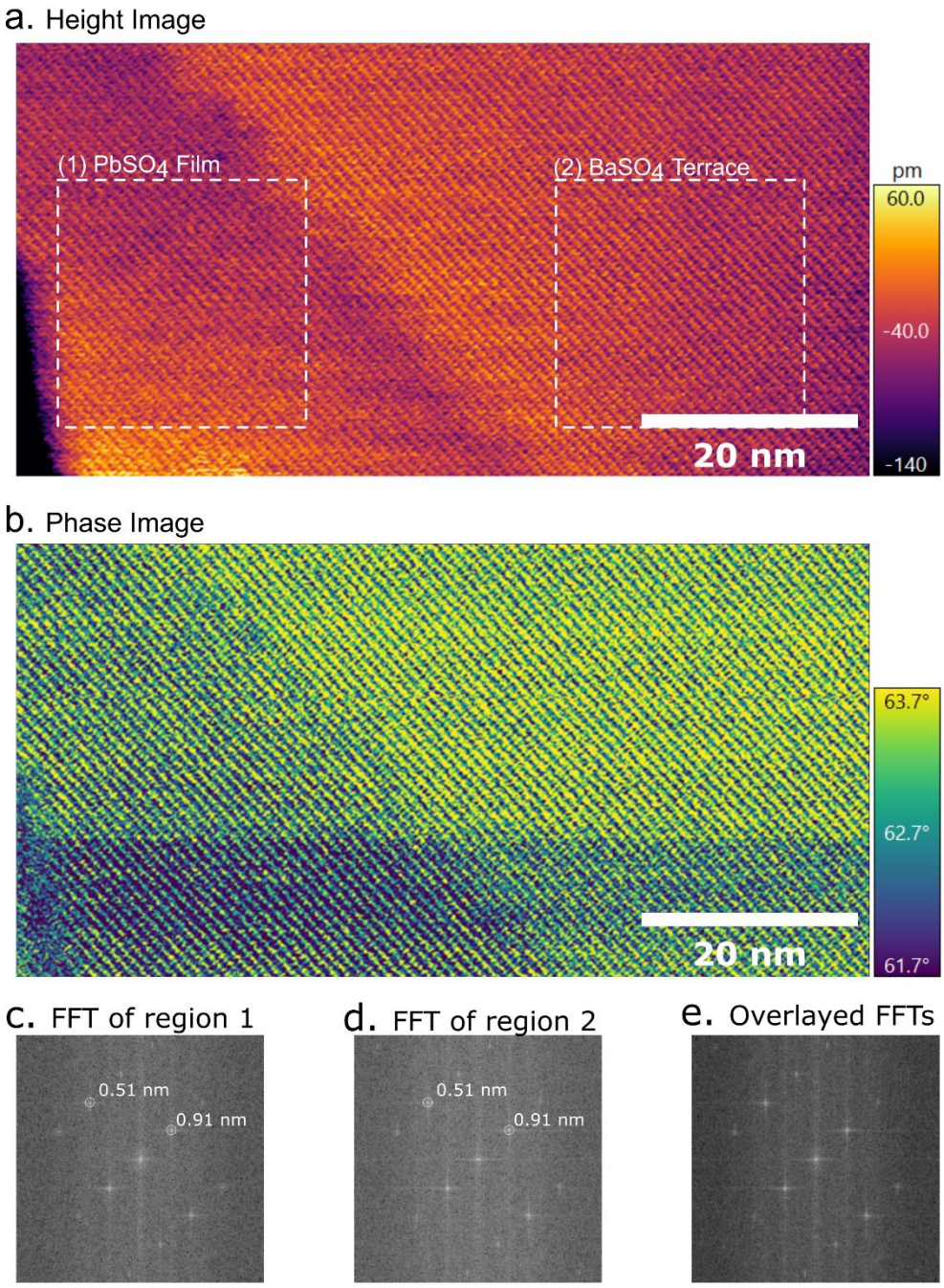

Figure S5: High-resolution AFM imaging shows the lattice periodicities of a barite surface with $PbSO_4$ overgrowth. *Subfigure **a.** shows a height-image. Subfigure **b.** shows a phase image of the same region. The left side of each image is a $PbSO_4$ monolayer that has grown from a step on the barite surface. The right side of each image shows a $BaSO_4$ terrace with no overgrowth. A very slight high difference (on the order of 20 pm) can be seen at the boundary between the two surfaces, which runs diagonally from left to right across the center of each image. The $PbSO_4$ terminated region also has a noticeably lower phase-shift than the $BaSO_4$ terminated surface. However, the lattice periodicities are identical for both surfaces, and are uninterrupted across the interface. Two regions (denoted 1 and 2, as marked in subfigure **a**) were analyzed using FFT. Subfigure **c.** shows the FFT of the PbSO4 monolayer film of region 1, and subfigure **d.** shows the FFT of the $BaSO_4$ terrace of region 2. Both regions show the same lattice periodicities of 0.51 nm and 0.91 nm. Subfigure **e.** is an additive overlay of both FFTs, showing their coincidence.*

6. X-ray Reflectivity Data Analysis

In situ high-resolution XR data were fit to a structural model consisting of solid barite, the interfacial solution near the barite (001) surface, and the bulk solution above this interfacial region. The bulk barite structure was modeled based on single-crystal X-ray diffraction results for crystals from the same source.[1] All atoms in the bulk crystal were fixed at their crystallographic positions except those in the top two unit-cell layers of the surface (i.e., ~14 Å depth from the top surface plane),[1] in which the atoms were allowed to relax along the surface normal direction (referred to as vertical relaxation). In this distorted barite region, the displacements of individual barium ions were determined independently whereas those of sulfate ions were determined as a group. Preliminary tests through our previous[1, 2] and current studies indicated that the specular XR data had relatively limited sensitivity to the relaxation of sulfate groups compared to those of barium ions.

The electron-density distribution of the species in the interfacial solution region was modeled using a Gaussian distribution defined by the occupation factor (o), height from the top barite surface (z, where z = 0 is defined as the location of the topmost Ba ion in the unrelaxed structure), and root-mean-square (rms) distribution width (u). The structure factor of solution species j at momentum transfer Q is expressed as

$$F_j(Q) = f^o(Q)\, o_j \exp(iQz_j) \exp(-Q^2u_j^2/2) \qquad \text{(Eq. I)}$$

where $f^o(Q)$ is the atomic form factor calculated from the database.[3] This calculation was conducted using the atomic form factor of oxygen, for simplicity and, to reflect the fact that the chemical composition of the interfacial solution is *in priori* unknown. The bulk solution structure above the interfacial region was expressed with the *layered water model*.[4]

Resonant anomalous X-ray reflectivity data were analyzed following the procedure described previously.[5] Briefly, the E-dependent anomalous dispersion, $f'(E)+if''(E)$, was derived using the differential Kramers-Kronig transform[6] of the Pb L_{III}-edge X-ray absorption spectrum measured in transmission mode through 0.1 M $Pb(NO_3)_2$ solution. The Q-dependent partial structure factor of Pb, $F_{Pb}(Q)$, was obtained initially using a model-independent approach[5] where $F_{Pb}(Q)$ is expressed using the amplitude, $A_{Pb}(Q)$, and phase, $\Phi_{Pb}(Q)$, as

$$F_M(Q) = A_{Pb}(Q) \exp(i\Phi_{Pb}(Q)) \qquad \text{(Eq. II)}$$

The derived model-independent results were used to yield a semi-quantitative electron-density profile of interfacial Pb whose detailed distribution was then modelled using a series of Gaussian distribution of Pb species as,

$$F_{Pb}(Q) = \Sigma_k\, \Gamma_{Pb,k} \exp(iQ\, z_{Pb,k}) \exp[-(Qu_{Pb,k})^2/2] \qquad \text{(Eq. III).}$$

with $\Gamma_{Pb,k}$, $z_{Pb,k}$, and $u_{Pb,k}$ are the coverage, height, and rms distribution width of the kth Pb species.

Various models were tested by changing the number of peaks in the interfacial region for each data set. The best-fit model was chosen based on the smallest χ^2 defined as

$$\chi^2 = [\Sigma_n(I_n - I_{calc,n})^2/\sigma_n^2]/(N - N_p) \quad \text{(Eq. IV)}$$

where N and N_p are the numbers of data points and parameters used in the model fit, respectively, I_n and $I_{calc,n}$ are the measured and calculated intensities, respectively, and σ_n is the uncertainty of the nth data point. The covariance among fitting parameters[7] was also considered and minimized to determine the optimal number of model parameters. The R-factor $(\Sigma_n|(I_n - I_{calc,n})/I_n|/N)$ of the best-fit is also reported for comparison.

The interfacial electron-density profile derived from the best-fit model is plotted as a function of height (z) from the surface. All electron-density profiles shown in this study are broadened by the experimental resolution (π/Q_{max}, where Q_{max} is the maximum Q of a dataset).

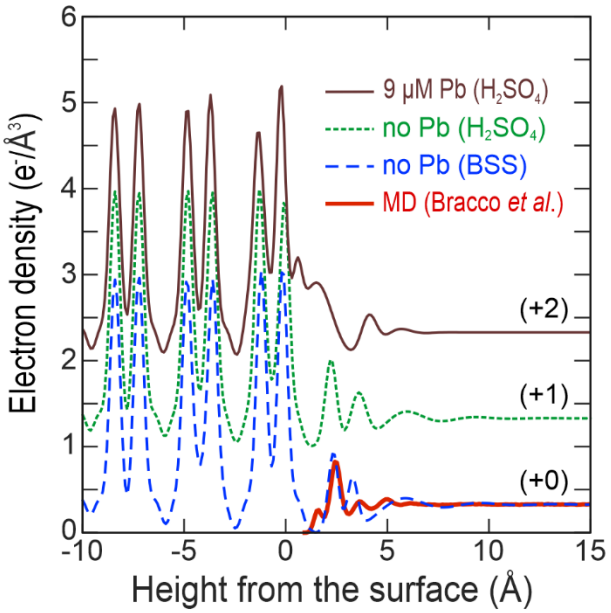

Figure S6: Electron density profiles obtained from fitting XR data to a structural model. *The best-fit model profiles are shown for 9 μM $Pb(NO_3)_2$ in 100 mM H_2SO_4, lead-free 100 mM H_2SO_4, and lead-free barite saturated solution (BSS). The solution structure of the BSS is compared with MD simulations of the BSS interfacial solution structure* from Bracco et al.[1].

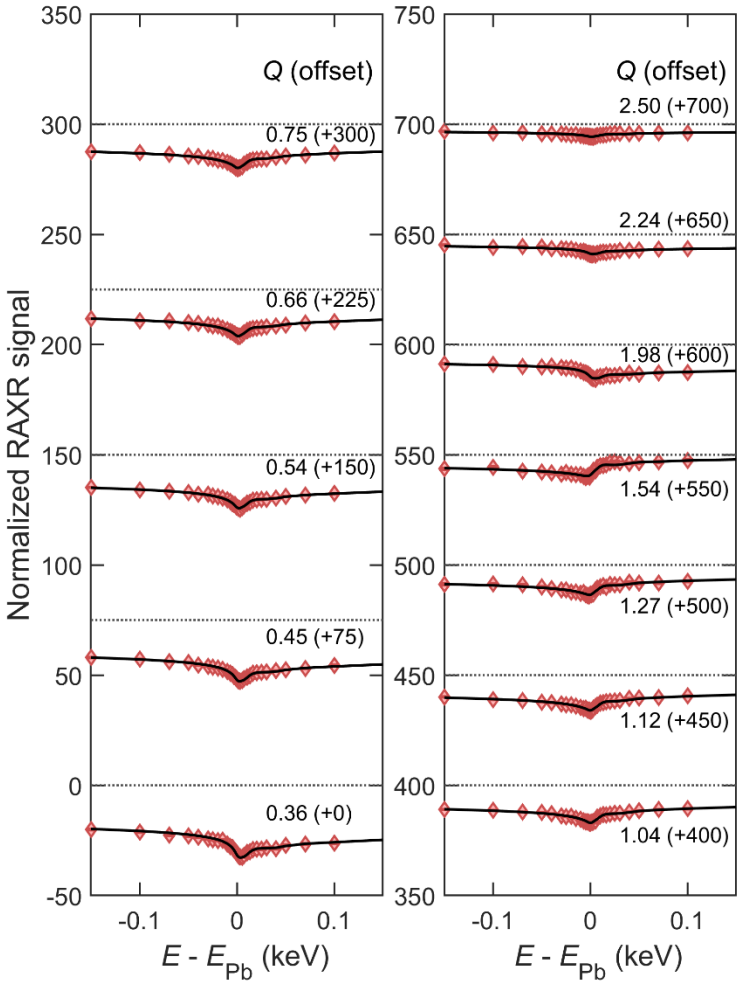

Figure S7: RAXR profiles obtained for barite (001) in the presence of 9 μM $Pb(NO_3)_2$ in 100 mM H_2SO_4. *RAXR profiles obtained for barite (001) in the presence of 9 μM $Pb(NO_3)_2$ in 100 mM H_2SO_4. The solid black curves are calculated from the best-fit model. The spectra are normalized based on the resonant amplitude normalization method ($(|F_{tot}(Q,E)|^2 - |F_{NR}(Q)|^2)/(2|F_{NR}(Q)|)$), where F_{tot} and F_{NR} are total and non-resonant structure factors, respectively.[7] The dotted horizontal lines are the reference spectra calculated for Pb-free systems. Each spectrum is labeled with Q ($Å^{-1}$) and the vertical offset of the spectrum in the parentheses.*

Table S1: Parameters of the best-fit model for RAXR data for barite (001) in 0.1 M H_2SO_4 containing 9 µM $Pb(NO_3)_2$.

Pb species	Parameters	Values
Incorporated Pb: total coverage: 2.72 ± 0.13 (Pb/A_{UC})		
	$\Gamma_{top,inc}$	1.22 ± 0.05 (Pb/A_{UC})
	$z_{top,inc}$	-0.69 ± 0.02 (Å)
	u_{inc}	0.55 ± 0.03 (Å)
	Δ_{inc}	3.45 ± 0.02 (Å)
	Λ_{inc}	5.8 ± 0.3 (Å)
Adsorbed Pb: total coverage: 1.08 ± 0.05 (Pb/A_{UC})		
	Γ_1	0.89 ± 0.03 (Pb/A_{UC})
	z_1	0.99 ± 0.03 (Å)
	u_1	0.64 ± 0.03 (Å)
	Γ_2	0.19 ± 0.04 (Pb/A_{UC})
	z_2	6.28 ± 0.12 (Å)
	u_2	1.11 ± 0.24 (Å)

$\Gamma_{top,inc}$ and $z_{top,inc}$: the coverage and height of Pb incorporated in the topmost solid layer; u_{inc} and Δ_{inc}: the rms distribution width and layer spacing of Pb incorporated in the solid; Λ_{inc}: exponential decay constant expressing the depth-dependent coverage variation of Pb incorporated in the solid; Γ_k, z_k, and u_k: the coverage, height, and rms distribution width of adsorbed Pb species k (where k = 1 and 2).

7. Atomistic modeling

Bulk $BaSO_4$ lattice parameters were computed using a cell with four formula units and a 4x3x2 k-points grid sample of the Brillion zone. An analogous bulk $PbSO_4$ simulation cell was initially relaxed to equilibrium. Subsequently, the $PbSO_4$ cell was constrained in the 'a' and 'b' directions to match the equilibrium $BaSO_4$ structure predicted by density functional theory (DFT) (a=5.569 Å and b=8.975 Å). To determine the new equilibrium value of the 'c' lattice of $PbSO_4$ layers on $BaSO_4$, the 'c' lattice parameter was varied around the unstrained original value, to locate the new minimum energy configuration. **Figure S8** shows the energy change with the 'c' lattice parameter.

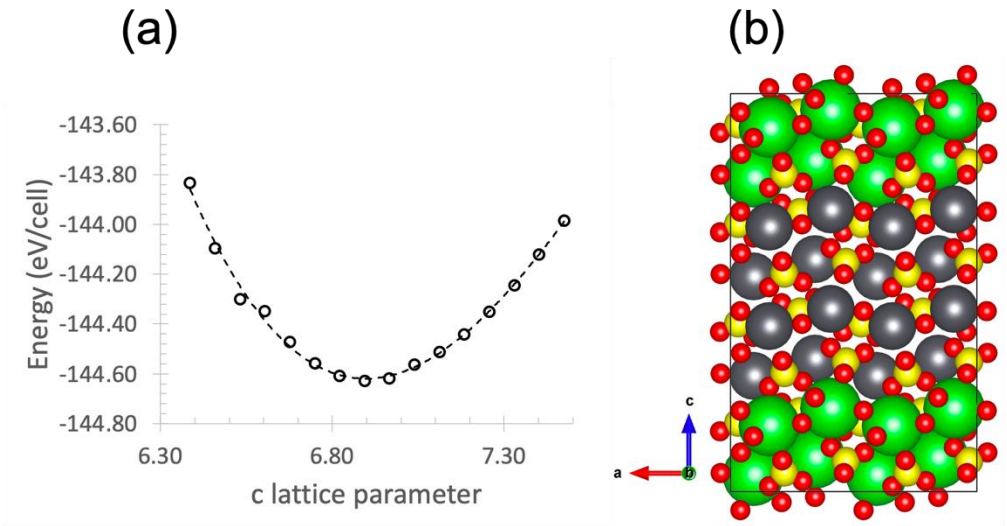

Figure S8: *(a) Energy change with c-lattice parameter (Å) of $PbSO_4$ constrained to the 'a' and 'b' lattice parameters of BaSO4. (b) schematic representation of the $PbSO_4$/$BaSO_4$ simulation cell used to compute interface energies. Green, gray, yellow and red spheres represent Ba, Pb, S and oxygen respectively.*

Having determined the relaxed c-lattice parameter, the energies of the strained and unstrained bulk $PbSO_4$ cells were the compared to determine the strain energy density per $PbSO_4$. The value of U_{nom} was then calculated as

$$U_{nom} = \frac{2(E_{bulk-PbSO_4-ab-strained} - E_{bulk-PbSO_4})}{\text{ab}} \qquad \text{(Eq. V)}$$

where:

U_{nom}: nominal strain energy density per unit area of monolayer film

$E_{bulk-PbSO_4-ab-strained}$: DFT computed energy of the strained $PbSO_4$ (per $PbSO_4$ unit)

$E_{bulk-PbSO_4-ab-strained}$: DFT computed energy of the unstrained $PbSO_4$ (per $PbSO_4$ unit)

a, b: lattice parameters that define the unit cell area, which contains two $PbSO_4$ units per monolayer.

A simulation cell with $PbSO_4$ between $BaSO_4$ was used to compute the interface energy between the two materials (see Figure S9b). The cell has 32 formula units of each material, with a total of 384 ions. The interfacial tension was computed as:

$$\gamma_{PbSO_4/BaSO_4} = \frac{\left(E_{BaSO_4+PbSO_4} - N_{BaSO_4}E_{bulk-BaSo_4} - N_{PbSO_4}E_{bulk-PbSO_4-ab-strained}\right)}{2A} \quad \text{(Eq. VI)}$$

where:

$\gamma_{PbSO_4/BaSO_4}$: Interfacial tension

$E_{BaSO_4+PbSO_4}$: DFT computed energy of the mixed $PbSO_4$/$BaSO_4$ interface-containing simulation cell.

N_{BaSO_4}: Number of $BaSO_4$ units in the interface-containing simulation cell.

N_{PbSO_4}: Number of $PbSO_4$ units in the interface-containing simulation cell.

$E_{bulk-BaSO_4}$: DFT computed fully relaxed energy of bulk $BaSO_4$ per $BaSO_4$ unit.

$E_{bulk-PbSO_4-ab-strained}$: DFT computed energy of ab-strained $PbSO_4$ per $PbSO_4$ unit.

A: Is the interfacial area of the simulation cell, which contains 2 interfaces.

Similar calculations were performed to determine the surface tensions of the strained and unstrained (001) surfaces, as calculated using Eq. VII:

$$\gamma_{XSO_4} = \frac{\left(E_{XSO_4\,(001)} - N_{BaSO_4}E_{bulk-XSo_4} - N_{PbSO_4}E_{bulk-XSO_4}\right)}{2A} \quad \text{(Eq. VII)}$$

where:

XSO_4: Represents either $PbSO_4$, $BaSO_4$, or ab-strained $PbSO_4$.

$E_{XSO_4\,(001)}$: DFT computed energy of the simulation slab cell including implicit solvent model (VASPsol).

$E_{bulk-XSO_4}$: DFT computed energy of the corresponding bulk cell, per SO_4 unit.

The interaction with the solvent was taking into account using the implicit solvent model VASPsol.[1] The model adds additional terms to the Kohn-Sham Hamiltonian taking into account the electrostatic interaction with a dielectric medium. The model is implemented in the DFT software Vienna Ab initio Software Package (VASP). The main modification to the code is the evaluation of the additional contributions to the total energy and the local potential.

The slab models have 80 formula units of the materials arranged in ten monolayers perpendicular to the (001) surface. Periodic boundary conditions were used for all calculations. There is a 20 Å thick vacuum space between repeating slabs in the direction perpendicular to the surface. Fig. S10 a and b show a schematic representation of the slab models for the pure $BaSO_4$ and $PbSO_4$.

The slab models to compute the monolayer and double layer of $PbSO_4$ on $BaSO_4$ were built by substituting Ba with Pb in each respective surface layer (see Figure S10 c and d).

The resulting energies are shown in Table S2.

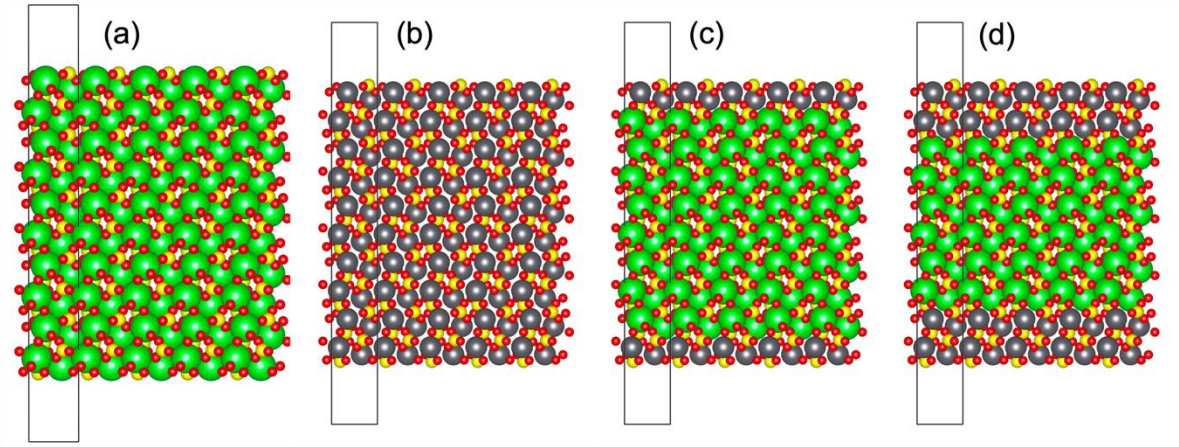

Figure S10: *Schematic representation of the slab surface models for (a) $BaSO_4$, (b) $PbSO_4$, (c) one monolayer of $PbSO_4$ on $BaSO_4$ and (d) a double layer of $PbSO_4$ on $PbSO_4$. Green, gray, yellow and red spheres represent Ba, Pb, S and oxygen respectively.*

Table S2: DFT computed simulation energies

System	Cell Dimensions (Å)			$BaSO_4$ units	$PbSO_4$ units	Energy per SO_4 units (eV)	Surface area (Å^2)	Surface tension (mJ/m^2)
	a	b	c					
Bulk $BaSO_4$	5.570	8.975	7.257	4	0	-39.33246		-
Bulk $PbSO_4$	5.439	8.662	7.025	0	4	-36.21994		-
Bulk $PbSO_4$ a-b strained	5.570	8.975	6.894	0	4	-36.15695	49.989	-
$BaSO_4$ (001)	11.139	17.951		80		-39.29689	199.954	γ_{BaSO_4} = 114
$PbSO_4$ (001)	11.139	17.951		0	80	-36.18989	199.954	γ_{PbSO_4} = 96
$PbSO_4$ (001) a-b strained	11.139	17.951		0	80	-36.08987	199.954	$\gamma^*_{PbSO_4}$ = 215
$BaSO_4$/$PbSO_4$ interface	5.570	8.975		8	8	-37.69617	49.989	$\gamma_{PbSO_4/BaSO_4}$ = 124
$BaSO_4$ (001) 1$PbSO_4$ layer	11.139	17.951		64	16	-38.65251	199.954	-
$BaSO_4$ (001) 2Pb layers	11.139	17.951		48	32	-37.83586	199.954	-

The excess chemical potential required to grow the first and second monolayers were calculated with reference to the chemical potential required to grow bulk $PbSO_4$ by comparing the energies of the one-monolayer and two-monolayer slabs shown in Fig S7c and d, with the energetics of the pure-barite slab (Fig S7a) and the bulk $PbSO_4$ and $BaSO_4$ simulations, as shown in Eq. IIX and IX.

$$\Delta\mu_{1PbSO_4} = \frac{\left(E_{BaSO_4(001)-1PbSO_4} - E_{BaSO_4(001)}\right)}{\Delta N_{PbSO_4}} - \left(E_{bulk-PbSO_4} - E_{bulk-BaSO_4}\right) \quad \text{(Eq. IIX)}$$

$$\Delta\mu_{2PbSO_4} = \frac{\left(E_{BaSO_4(001)-2PbSO_4} - E_{BaSO_4(001)-1PbSO_4}\right)}{\Delta N_{PbSO_4}} - \left(E_{bulk-PbSO_4} - E_{bulk-BaSO_4}\right) \quad \text{(Eq. IX)}$$

where:

$\Delta\mu_{1PbSO_4}$: is the excess chemical potential required to grow the first monolayer on pure barite

$\Delta\mu_{1PbSO_4}$: is the excess chemical potential required to grow a second monolayer on an existing monolayer.

ΔN_{PbSO_4}: is the difference in number of $PbSO_4$ units between the two slab simulations.

The resulting energies are shown in Table S3, where they are also compared with the energy required to grow unstrained $PbSO_4$ and bulk strained $PbSO_4$.

Table S3: DFT-based energy calculations

System	eV/$PbSO_4$	Saturation to drive growth $\boldsymbol{\sigma = \ln\left(\{Pb^{2+}\}\{SO_4^{2-}\}/K_{sp}\right)}$
Bulk $PbSO_4$	0	0
Strained $PbSO_4$	0.063	9.73
First Layer Epitaxial PbSO4	0.109	4.22
Second Layer Epitaxial $PbSO_4$	0.971	37.5

8. Effect of prior film growth on future film growth

As described in the main text, a series of AFM experiments was performed to test the influence of film growth on incorporation of Pb into the underlying substrate. In this experiment, a $PbSO_4$ film was grown over part of the barite surface using a 6 µM $Pb(NO_3)$ 100 mM H_2SO_4 solution, then partially dissolved away using a lead-free 100 mM H_2SO_4 solution, and then regrown. The image sequences described there are shown in **Figure S11.**

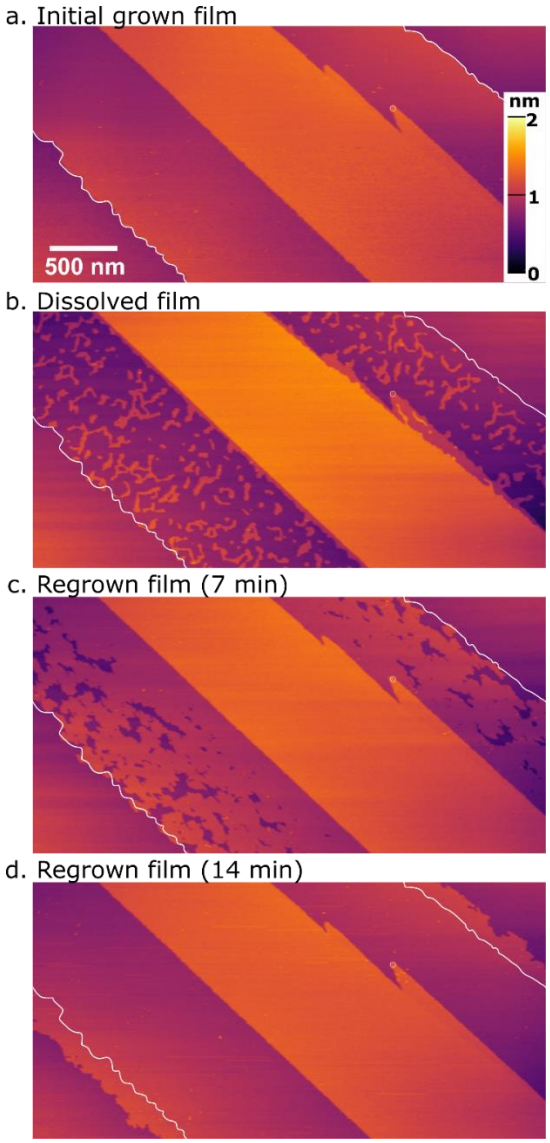

Figure S11: Film-regrowth series. a. *shows an initial film which was grown across the surface from a 6 µM $Pb(NO_3)_2$ + 100 mM H_2SO_4 solution. A white line has been added to designate the furthest distance of advance for the film. The central terrace is a barite terrace with no $PbSO_4$ film. On either side, there is a grown PbSO4 terrace that is ~500-800 nm wide) that has propagated from the step edges of the central barite terrace. Outside of the white lines is another region of barite terrace.* ***b****. Shows the residual islands after most of the film has been dissolved in lead-free 100 mM H_2SO_4.* ***c****. Shows the surface after the film has regrown for 7 minutes in 6 µM $Pb(NO_3)_2$ + 100 mM H_2SO_4. The film is seen to regrow fastest over the areas that are closer to the step edge (and hence were capped sooner during initial growth).* ***d****. shows the surface after the film has regrown for a total of 14 minutes. Here we finally see the slow propagation of the film into regions of the surface that had never been capped during the initial film growth.*

9. Exposure to high concentrations of $PbSO_4$

An AFM experiment was performed while imaging the barite (001) surface when exposed to increasingly higher concentrations of Pb^{2+}. Solutions were prepared by mixing 100 mM H_2SO_4 solution with small amounts of 1 mM $Pb(NO_3)_2$ to obtain lead concentrations from 9 µM up to 360 µM. These experiments were meant to test whether it was possible to drive multilayer growth by increasing supersaturation.

When concentrations of 90 µM $Pb(NO_3)_2$ or higher were used, we did observe the nucleation of bulk $PbSO_4$ crystals directly from bulk solution. This was visible in optical microscopy (which allow us to survey large regions of surface (Fig. S7). Many of these crystals were weakly-adhered flocs that deposited onto the surface and moved in response to fluid-flow. However, there were some crystals that preferentially adhered to and/or formed on optically-visible 'macrosteps.' These macrosteps are locations where other crystallographic faces of the barite surface would be exposed. This is clearly seen in Fig. S7, and it is also consistent with anglesite crystals that have grown on macroscopic step-edges with apparent preferential crystallographic orientation with respect to the substrate barite as shown in Figure S4.

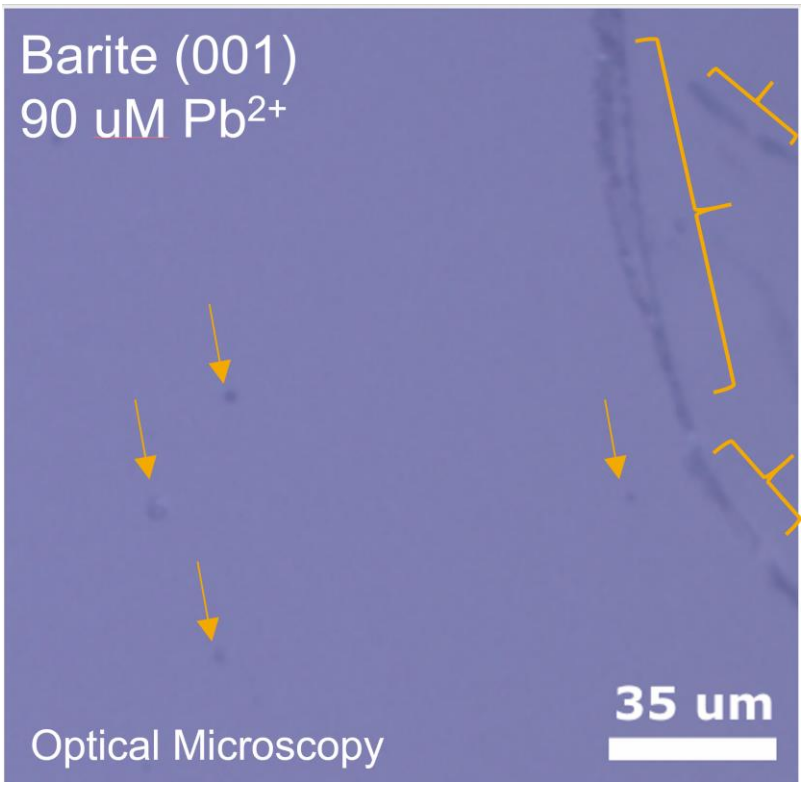

Figure S12: *Optical image of the barite surface, imaged in 90 µM Pb2+ solution. Larger particles (indicated by orange arrows) are observed in rare locations on the surface. Many of these are mobile under flow. Larger concentrations of particles are seen on surface defects (including macrosteps), as highlighted by orange brackets.*

However, the high-resolution images of typical (001) surface areas without such macrosteps show that epitaxial multilayer-growth is highly suppressed. Our AFM image series in increasing concentrations of lead (Fig. S8) showed formation of a monolayer, as expected in the presence of 9 µM $Pb(NO_3)_2$. However, there was essentially no change in surface structure as the concentration is increased from 9 µM to 360 µM, despite the nearly 40-fold increase in saturation. This is especially

remarkable, since the presence of existing step-edges should enable rapid advancement if growth of a second layer were thermodynamically favorable. However, no step-edge advancement is observed. Thus, we conclude that epitaxial multilayer growth is strongly inhibited. (Note that this image-sequence, there are some visible rod-like particles or 'streaks' on the barite surface. These are believed to be small organic molecules such as adventitious carbon that adsorbed onto the surface.).

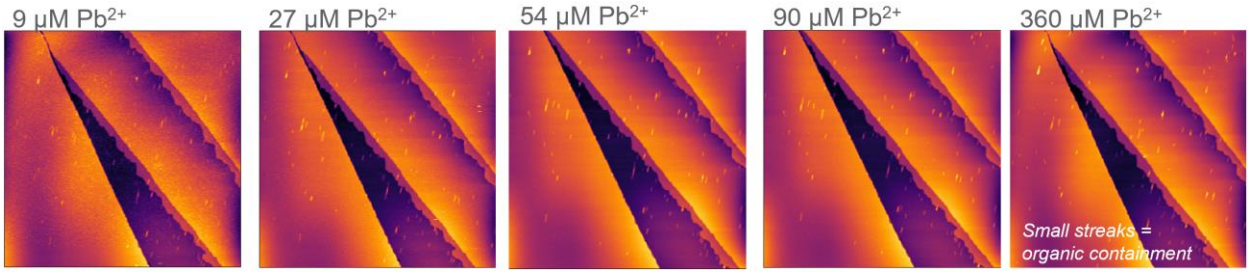

Figure S13: *Concentration series obtained with lead concentrations from 9 µM up to 360 µM. Growth of a single $PbSO_4$ monolayer is observed in 9 µM Pb^{2+} solutions, but no additional growth is observed, even at the highest concentrations. Image sizes are each 1 µm x 1 µm.*

10. Strain Analysis

When estimating the strain energy density of an epitaxial $PbSO_4$ thin film on barite (001), we utilize Eq. 1 of the main text. The epitaxial strains are estimated as $\varepsilon_1 = \ln\frac{a_{PbSO4}}{aBaSO_4} = -0.047$ and $\varepsilon_2 = \ln\frac{b_{PbSO4}}{b_{BaSO4}} = -0.011$, with lattice parameters from ref 8. In place of the stiffness tensor for anglesite, which is unknown, we substitute the stiffness tensor for barite from ref 9, with $c_{11} = 106.9$ GPa, $c_{22} = 71.8$ GPa, $c_{33} = 101.8$ GPa, $c_{12} = 32.4$ GPa, $c_{13} = 29.7$ GPa, $c_{23} = 24.3$ GPa). This leads to an estimated strain energy of a $PbSO_4$ monolayer on $BaSO_4$ at $U_{nom}^{PbSO_4/BaSO_4} = 36\frac{\mathrm{mJ}}{\mathrm{m}^2}$, which can alternatively be expressed as a strain energy density of 5.3 kJ/mol.

For $PbSO_4$ on barite (001), we have $\varepsilon_1 = \ln\frac{a_{PbSO4}}{aBaSO_4} = -0.047$ and $\varepsilon_2 = \ln\frac{b_{PbSO4}}{b_{BaSO4}} = -0.011$. ($c_{11} = 106.9$ GPa, $c_{22} = 71.8$ GPa, $c_{33} = 101.8$ GPa, $c_{12} = 32.4$ GPa, $c_{13} = 29.7$ GPa, $c_{23} = 24.3$ GPa), from which we estimate the strain energy of a $PbSO_4$ monolayer on $BaSO_4$ at $U_{nom}^{PbSO_4/BaSO_4} = 36\frac{\mathrm{mJ}}{\mathrm{m}^2}$, corresponding to a strain energy density of 5.3 kJ/mol.

11. $PbSO_4$ Saturation Analysis.

Calculations of $PbSO_4$ solubility and $PbSO_4$ saturation were obtained using Visual MINTEQ 3.0 using the default thermodynamic databases and standard settings[10], including the following parameters:

Method for activity correction: *Davies*
Davies b parameter: *0.3*
pH: *calculated from mass balance*
Ionic strength: *to be calculated*

To estimate the solubility of $PbSO_4$ in 100 mM H_2SO_4, a calculation was performed with initial composition of 200 millimolal H^+ and 100 millimolal SO_4^{-2}, with anglesite set as an infinite solid phase. (The standard units for aqueous speciation calculations are molality. The small differences between molal and molar scales are neglected here for simplicity). These calculations produce a solution in equilibrium with respect to anglesite (i.e. saturation index = 0). The predicted solution speciation is shown in Table S4, while the summarized equilibrated mass distributions are shown in Table S5. This show an Pb^{2+} solubility of 15.699 micromolal, which we approximate in the main text as 16 μM.

Table S4: MINTEQ Predicted solution speciation of a 100 millimolal H_2SO_4 after equilibration with Anglesite.

	Concentration	Activity	Log activity
H+1	1.2012E-01	9.1603E-02	-1.038
HSO4-	7.9890E-02	6.0925E-02	-1.215
OH-	1.4414E-13	1.0992E-13	-12.959
Pb(OH)2 (aq)	2.2144E-21	2.2871E-21	-20.641
Pb(OH)3-	3.2967E-31	2.5141E-31	-30.600
Pb(SO4)2-2	9.6307E-07	3.2575E-07	-6.487
Pb+2	7.0450E-06	2.3829E-06	-5.623
Pb2OH+3	2.8480E-16	2.4849E-17	-16.605
Pb3(OH)4+2	7.3530E-37	2.4871E-37	-36.604
Pb4(OH)4+4	4.5277E-38	5.9266E-40	-39.227
PbOH+	8.6277E-13	6.5796E-13	-12.182
PbSO4 (aq)	7.6909E-06	7.9433E-06	-5.100
SO4-2	2.0121E-02	6.8059E-03	-2.167

Table S5: MINTEQ Predicted Equilibrated Mass Distributions for 100 mmolal H_2SO_4 after equilibration with Anglesite

Component	Total dissolved	% dissolved	Total sorbed	% sorbed	Total precipitated	% precipitated
H+1	2.0001E-01	100.000	0	0.000	0	0.000
Pb+2	1.5699E-05	100.000	0	0.000	0	0.000
SO4-2	1.0002E-01	100.000	0	0.000	0	0.000

A second calculation was performed to predict the saturation state of the standard experimental solutions, containing 9 μM $Pb(NO_3)_2$ in 100 mM H_2SO_4. The same default settings were used, but the composition was fixed at 200 mM H^+, 100 millimolal SO_4^{-2}, 0.009 millimolal Pb^{2+}, and 0.018 millimolal NO_3^-. No solid phases were allowed to form. The predicted solution speciation is shown in Table S6, and the predicted solution saturations are shown in Table S7. The calculations predict that the solution is subsaturated with respect to all relevant phases, including anglesite, as denoted by the negative Sat. Index. Note that the Sat. Index defined by MINTEQ is defined using a base-10 log scale, and is thus a factor of 2.3 smaller in magnitude than the saturation parameter, σ, which we employ in the main text and which is defined using a natural log scale.

Table S6: MINTEQ predicted solution speciation of a solution of 100 millimolal H_2SO_4 and 9 µmolal $Pb(NO_3)_2$.

	Concentration	Activity	Log activity
H+1	1.2012E-01	9.1608E-02	-1.038
HSO4-	7.9877E-02	6.0916E-02	-1.215
NO3-1	1.8000E-05	1.3727E-05	-4.862
OH-	1.4413E-13	1.0992E-13	-12.959
Pb(NO3)2 (aq)	6.2609E-15	6.4664E-15	-14.189
Pb(OH)2 (aq)	1.2695E-21	1.3112E-21	-20.882
Pb(OH)3-	1.8898E-31	1.4412E-31	-30.841
Pb(SO4)2-2	5.5193E-07	1.8669E-07	-6.729
Pb+2	4.0391E-06	1.3662E-06	-5.864
Pb2OH+3	9.3613E-17	8.1679E-18	-17.088
Pb3(OH)4+2	1.3855E-37	4.6863E-38	-37.329
Pb4(OH)4+4	4.8913E-39	6.4026E-41	-40.194
PbNO3+	3.6373E-10	2.7739E-10	-9.557
PbOH+	4.9463E-13	3.7721E-13	-12.423
PbSO4 (aq)	4.4085E-06	4.5532E-06	-5.342
SO4-2	2.0117E-02	6.8045E-03	-2.167

Table S7: MINTEQ predicted saturation indices of a solution of 100 millimolal H_2SO_4 and 9 µmolal $Pb(NO_3)_2$.

Mineral	$\log_{10}$ IAP	Sat. Index = $\log_{10}$ IAP- log K_s	Mineral Stoichiometry							
Anglesite	-8.032	-0.242	1	Pb+2	1	SO4-2				
Larnakite	-11.820	-11.386	-2	H+1	2	Pb+2	1	SO4-2	1	H2O
Litharge	-3.788	-16.478	1	Pb+2	1	H2O	-2	H+1		
Massicot	-3.788	-16.678	1	Pb+2	1	H2O	-2	H+1		
Pb(OH)2(s)	-3.788	-11.938	-2	H+1	1	Pb+2	2	H2O		
Pb2O(OH)2(s)	-7.577	-33.767	2	Pb+2	3	H2O	-4	H+1		
Pb3O2SO4(s)	-15.608	-26.295	-4	H+1	3	Pb+2	1	SO4-2	2	H2O
Pb4(OH)6SO4(s)	-19.397	-40.497	-6	H+1	4	Pb+2	1	SO4-2	6	H2O
Pb4O3SO4(s)	-19.397	-41.274	-6	H+1	4	Pb+2	1	SO4-2	3	H2O
PbO:0.3H2O(s)	-3.788	-16.768	-2	H+1	1	Pb+2	1.33	H2O		

12. Supporting References

(1) Bracco, J. N.; Lee, S. S.; Stubbs, J. E.; Eng, P. J.; Heberling, F.; Fenter, P.; Stack, A. G. Hydration Structure of the Barite (001)–Water Interface: Comparison of X-Ray Reflectivity with Molecular Dynamics Simulations. *The Journal of Physical Chemistry C* **2017**, *121* (22), 12236-12248.
(2) Bracco, J. N.; Lee, S. S.; Braha, I.; Dorfman, A.; Fenter, P.; Stack, A. G. Pb Sorption at the Barite (001)–Water Interface. *The Journal of Physical Chemistry C* **2020**, *124* (40), 22035-22045.
(3) Wilson, A. J. C. *International Tables for Crystallography, Vol. C: Mathematical, Physical, and Chemical Tables*; Dordrecht: Kluwer Academic Publishers, 1992.
(4) Schlegel, M. L.; Nagy, K. L.; Fenter, P.; Cheng, L.; Sturchio, N. C.; Jacobsen, S. D. Cation Sorption on the Muscovite (001) Surface in Chloride Solutions Using High-Resolution X-Ray Reflectivity. *Geochim. Cosmochim. Acta* **2006**, *70*, 3549-3565.
(5) Park, C.; Fenter, P. A. Phasing of Resonant Anomalous X-Ray Reflectivity Spectra and Direct Fourier Synthesis of Element-Specific Partial Structures at Buried Interfaces. *J. Appl. Crystallogr.* **2007**, *40*, 290-301.
(6) Cross, J. O.; Newville, M.; Rehr, J. J.; Sorensen, L. B.; Bouldin, C. E.; Watson, G.; Gouder, T.; Lander, G. H.; Bell, M. I. Inclusion of Local Structure Effects in Theoretical X-Ray Resonant Scattering Amplitudes Using *Ab Initio* X-Ray-Absorption Spectra Calculations. *Phys. Rev. B: Condens. Matter* **1998**, *58*, 11215-11225.
(7) Lee, S. S.; Park, C.; Fenter, P.; Sturchio, N. C.; Nagy, K. L. Competitive Adsorption of Strontium and Fulvic Acid at the Muscovite-Solution Interface Observed with Resonant Anomalous X-Ray Reflectivity. *Geochim. Cosmochim. Acta* **2010**, *74*, 1762-1776.
(8) Miyake, M.; Minato, I.; Morikawa, H.; Iwai, S. Crystal Structures and Sulphate Force Constants of Barite, Celestite, and Anglesite. *American Mineralogist* **1978**, *63* (5-6), 506-510.
(9) Santamaría-Pérez, D.; Kumar, R. S.; Dos Santos-Garcia, A.; Errandonea, D.; Chulia-Jordan, R.; Saez-Puche, R.; Rodríguez-Hernández, P.; Muñoz, A. High-Pressure Transition to the Post-Barite Phase in Bacro 4 Hashemite. *Physical Review B* **2012**, *86* (9), 094116.
(10) Gustafsson, J. P. Visual Minteq 3.0 User Guide. *KTH, Department of Land and Water Recources, Stockholm, Sweden* **2011**.